UNIVERSITY OF CALGARY

Tapered optical nanofiber

for light-atom interfacing

by

Aveek Chandra

A THESIS

SUBMITTED TO THE FACULTY OF GRADUATE STUDIES

IN PARTIAL FULFILLMENT OF THE REQUIREMENTS FOR THE

DEGREE OF MASTER OF SCIENCE

DEPARTMENT OF PHYSICS AND ASTRONOMY

CALGARY, ALBERTA

August, 2014

Abstract

This project aims to develop scientific as well as technical foundations towards realization of a novel platform for light-matter interaction based on tapered optical nanofibers that enable to interface neutral atoms in their vicinity. A setup for magneto-optical trap (MOT) has been built. Tapered nanofibers (TNFs) of sub-wavelength diameter, with transmission of 95% have been fabricated and characterized. Next, a nanofiber is transferred into the MOT setup and installed inside the vacuum chamber. The MOT cloud and nanofiber are made to spatially overlap inside ultra-high vacuum (UHV). Coupling of fluorescence of MOT into the guided mode of TNF has been observed. This clearly shows the coupling of atoms with the fiber-guided mode and that our interface works. In addition, $65 - 70\%$ absorption of a free space beam by the atomic cloud has been observed and the relevant MOT parameters are obtained from it. Our efforts are directed towards observing interaction of atoms with the fiber-guided light via evanescent field. Attempts have been made to observe absorption of a probe beam through the nanofiber by the MOT cloud and techniques for switching on-off the MOT beams, the probe beam and the magnetic field are developed for that purpose.

Ultimately, the goal will be to trap atoms in the vicinity of a nanofiber enabling to reach a large optical depth accompanied by the ability to reach high intensities for low optical power. I will present my work on the development of this MOT-nanofiber interface - a new promising platform for research in nonlinear quantum optics, quantum information science and technology, quantum communication and hybrid quantum system.

Acknowledgements

I would like to gratefully acknowledge the guidance and support of my supervisor, Alex Lvovsky. I would like to thank him for giving me the opportunity to work with him at Institute for Quantum Science and Technology. I am grateful to Dr. Paul Barclay for sharing his fiber-pulling facilities with us. There would be no tapered fiber without his entire group's support. Many thanks to Nicolas R, Matt M, Marcelo W, Behzad K, Chris H, David L, Hamidreza K and Harishankar J.

I have had amazing co-workers and mentors in the last couple of years. Andrew M, Connor K and Ryan T are the guys I looked up to when I joined Lvovsky group. I express my gratitude to Dr. Arturo Lezama for getting us together and starting the project. I have had the pleasure of working with : Di C, Tayebe N, Vinay A I, Travis B, Eugene M and Dr. Andal N. Special thanks to all of them.

With the love and care of my family back home, and my friends here, I have braved and enjoyed Calgary in her rugged mountains and white snowfields. I would always remember Calgary as the place where I grew up. Things would not have been the same, without my dear friends - Abhirup and Di and without my outdoor activity buddy - Travis.

I would like to thank my other colleagues: Pan P, Daniel H, Adarsh S P, Zhongzhong Q, Arina T, Daniel O who have helped me in many different ways. My sincere regards to Edward C in electronic shop and Andy R in scientific workshop for their technical help and advice.

Aveek Chandra

Calgary, August 2014.

Table of Contents

List of Tables

List of Figures and Illustrations

List of Symbols, Abbreviations and Nomenclature

Symbol	Definition
U of C	University of Calgary
TNF	Tapered nanofiber
UHV	Ultra-high vacuum
MOT	Magneto-optical trap
EIT	Electromagnetically induced transparency
XPM	Cross phase modulation
IPA	Isopropyl alcohol
SPCM	Single photon counting module
APD	Avalanche photodiode
TA	Tapered amplifier
PD	Photodetector
VCO	Voltage controlled oscillator
IGBT	Insulated gate bipolar transistor
AOM	Acousto-optic modulator
ECDL	External cavity diode laser
PBS	Polarizing beam splitter
TTL	Transistor-transistor logic
SEM	Scanning electron microscope
PMF	Polarization maintaining fiber

Chapter 1

Introduction

The light-matter interaction at the fundamental level, where a single photon interacts with a single atom, has been a topic of extensive research over last two decades [1, 2, 3, 4]. Since the resonant absorption cross-section of an atom is of the order $\sim \lambda^2$, where λ is the wavelength of the absorbed light, such an interaction is generally weak. Many approaches are taken to enhance this interaction. One possibility is to enhance the atomic densities [5, 6], another possibility is to modify or tailor the light field for an effective stronger interaction. In this context, resonant structures [7, 8] ranging from cavities to micro and nano structures are widely used to facilitate light-atom interfacing. For instance, a photon trapped inside a high finesse cavity passes through the position of an atom a million times before it leaks out from the cavity and thereby increasing the coupling strength [9]. In this regard, dielectric structures such as micro-resonators have also been employed in recent years [10].

The development of miniaturized and integration technologies as well as fabrication techniques have ushered in new ways of combining different quantum systems leading to realization of hybrid quantum systems [11]. In the field of quantum science and technology, there are efforts to realize quantum networks [12], which will have quantum nodes where single photons can be stored and locally manipulated. The quantum nodes will be connected by quantum channels for transfer of information between them. In our case, we have an ensemble of trapped cold atoms in magneto-optical trap (MOT) and we are trying to interact with these atoms through the evanescent field of a tapered optical nanofiber (TNF), which is fabricated from a regular commercial fiber. Our experiment can be a promising step towards realizing such a quantum network, with the ensemble of atoms representing the node while the optical fiber represents the quantum channel.

In quantum-optical science and technology, there is an interest to realize nonlinear interaction at single photon energy levels. This will lead to unconditional universal quantum computing with photons [13] as well as methods for preparation and measurement of photon number states. The most sought after quantum gate is the controlled-phase gate where the phase of one photon shifts the phase of another photon by π. This phenomenon of cross-phase modulation (XPM) has been observed but it is still far from the desired π phase shift [50]. A scheme for creating large XPM based on electromagnetically induced transparency (EIT) has been proposed by Schmidt and Imamoglu [27] almost two decades ago. This scheme has shown that arbitrarily large XPM can be created without the hindrance of absorption, however the phase shift is limited by the effect of the pulse bandwidth [28] and its transverse mode [29]. One of the long-term goals of our experiment is to implement non-linear optical interaction at single photon energy levels based on this Schmidt-Imamoglu scheme.

In order to enhance non-linear effects of a system, two criteria can be exploited - one of which is the nonlinearity of the medium and the other is the intensity of light used. The optical depth of a medium, OD, is a dimensionless quantity which quantifies the strength of the interaction between the medium and light such that $OD = \eta\sigma L$, where η is the density of the medium , σ is the absorption cross-section of the atoms in the medium and L is the interaction length.

In an atomic system, η is limited because of the dephasing effects arising from atomic collisions at high densities. For maximizing σ, the alkali atoms are chosen as they offer the largest absorption cross-sections available. Therefore, the obvious way to increase the optical depth is by increasing the interaction length L. Optical nanofibers offer an ideal way by which this can be achieved as the evanescent field interacts with the surrounding medium over the taper length (typically several mm). This is in contrast to the interaction that can be achieved by a tightly focussed laser beam, where the length of the interaction is limited by the diffraction of the beam. For example, a laser beam focussed to a waist of 2.3 μm

interacting with cold Cs atoms (transition wavelength $\sim$ 850 nm) has a Rayleigh length of 20 μm, few orders of magnitude smaller than few mm interaction length offered by optical nanofibers.

The other parameter that can be optimized is the laser beam intensity. In principle, the beam mode area should be proportional to the wavelength of the light in order to maximize the available intensity. This can be achieved by tightly focussing a free-space beam, however in doing so, the interaction length, L is reduced. The optical nanofiber with sub-wavelength diameter offers an ideal platform for reaching high intensities while maintaing a relatively long interaction length. Since the mode is confined within the evanescent field, high intensities can be achieved for low input power (order of mW or less). Therefore, optical nanofibers embedded in atomic systems may be an ideal tool for studies in nonlinear quantum optics.

A TNF is fabricated by heating and stretching a commercial fiber, bringing its radius down to few hundreds of nanometers. Such a fiber offers a strong transverse confinement of the guided mode while exhibiting a pronounced evanescent field surrounding its tapered region. This allows atoms in the vicinity (at sub-micron distances from the surface) of TNF to be addressed by the light propagating through the fiber.

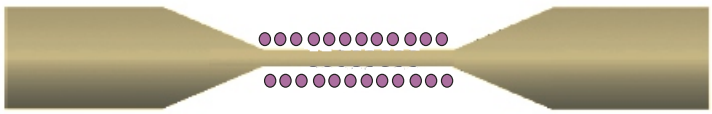

Figure 1.1: Trapping of atoms in the vicinity of a tapered nanofiber. Large optical depths can be achieved in this interface

Ultimately in this system, the goal will be to trap atoms in the vicinity of the nanofiber for controlled light-matter interaction. The method of trapping has been elaborated by

Vetsch et. al [41] following a proposal by Kien et. al. [31, 32]. A red-detuned laser field will be sent through the nanofiber creating a dipole attractive potential. This field will hold the atoms from drifting away from the nanofiber surface. However, the atoms can fall onto the TNF surface because of van der Waals attraction from fiber surface. In order to prevent this from happening, another laser field, blue-detuned from the atomic resonance is transmitted through the nanofiber. The blue-detuned evanescent field has a shorter decay length than the red-detuned field such that the atoms will be repelled away from the fiber surface. Therefore, the atoms will be trapped around the nanofiber (shown in Fig. 1.1) without touching it. The red-detuned field is usually a standing wave to prevent the uncontrolled longitudinal drifting of atoms. The atoms are trapped longitudinally at the points of minimum potential around the nanofiber. This scheme will enable us to reach large optical densities, which implies strong light-atom interaction. Such an atom trapping scheme has been implemented by the groups of A. Rauschenbeutel [22] in 2010, reaching an optical density of 32, and J. Kimble [39] in 2012, reaching an optical density of 66. Once atoms are trapped around nanofiber, one can perform a vast majority of experiments. The ones that are of interest to me are:

- Development of an optical quantum memory for reversible storage and retrieval of single-photons. The storage can be realized using the electromagnetically-induced transparency (EIT) technique.
- Exploration of optical nonlinearity at single photon energy levels (i.e XPM) by Schmidt and Imamoglu proposal.
- Creation of a high-efficiency fiber-coupled-single-photon source. A scheme proposed by Duan, Lukin, Cirac and Lukin (commonly referred to as DLCZ protocol) [5] in 2001, is a remarkable way to generate single photons from a large ensemble of atoms.

- The interface can be used for coupling addressable atoms with solid state devices. It would be interesting to investigate the coupling between trapped atoms and a Bragg reflector (cavity QED) or an optomechanical resonator (hybrid quantum system).

The advantage of a fiber-atom interface is that quantum information can be stored and transferred over long distances with minimal loss and hence it can be used as a tool for experiments on quantum communication.

In this thesis, I will present my work on building such a MOT-nanofiber interface from scratch. We have assembled the setup for magneto-optical trap. We have fabricated as well as characterized the tapered nanofibers. The MOT cloud and the nanofiber are overlapped inside ultra-high vacuum (UHV) and atomic fluorescence of the MOT through the nanofiber is observed. This clearly shows the coupling of atoms with the fiber-guided mode and that our interface works. Attempts have been made to see the absorption of a probe beam through the nanofiber by the MOT cloud. Experimental techniques for switching on-off the MOT beams, the probe beam and the magnetic field have been developed for that purpose. The experimental difficulties that are faced in this experiment are discussed. Finally, some ways of making further development and progress in our experiment have been suggested.

I will start with a theoretical discussion on propagation of light in step-index optical fibers and nanofibers in Chapter 2. Chapter 3 will talk about the principles of magneto-optical trap and some of its features. Chapter 4 will be entirely devoted to nanofibers - its characteristization, and some technical aspects starting from fabrication to installation inside the vacuum chamber. The details of our experimental setup and methods will be discussed in Chapter 5. Finally, I will conclude my thesis in Chapter 6 with my comments on improvement of our current setup and future research directions.

Chapter 2

Light propagation in step-index optical fiber and tapered nanofiber

Optical fibers are widely used for telecommunication because they allow transmission of light with minimal loss over large distances. They have a circular core-cladded structure (Fig. 2.1). Light rays when incident on the core-cladding boundary at angles greater than critical angles undergo total internal reflection and are guided through the core along the fiber. The core is typically made of silica (SiO_2) doped with germanium or fluorine and the cladding of silica. The core has 1% higher refractive index than the cladding because of which light in the core penetrates deep into the cladding as evanescent (or exponentially decaying) wave. Therefore, a thick layer of cladding is required for isolation of the guided light from the surrounding. The ratio between the radius of core and cladding is typically between 1/30 and 1/10 in standard commercial fibers.

When the diameter of core is small such that only a single mode is allowed to propagate, then the fiber is called **single mode fiber**. Fibers with large core diameters allow propagation of many modes together and are called **multimode fibers**. Each mode is characterized by its propagation constant, group velocity, polarization and a transverse spatial distribution. In this chapter, I will discuss light propagation in optical fiber and tapered nanofiber.

2.1 Solution for the fields in an optical fiber

From Maxwell's equations, one can derive the wave equations in cylindrical coordinates. These equations are then applied to the core and cladding regions to obtain separate solutions

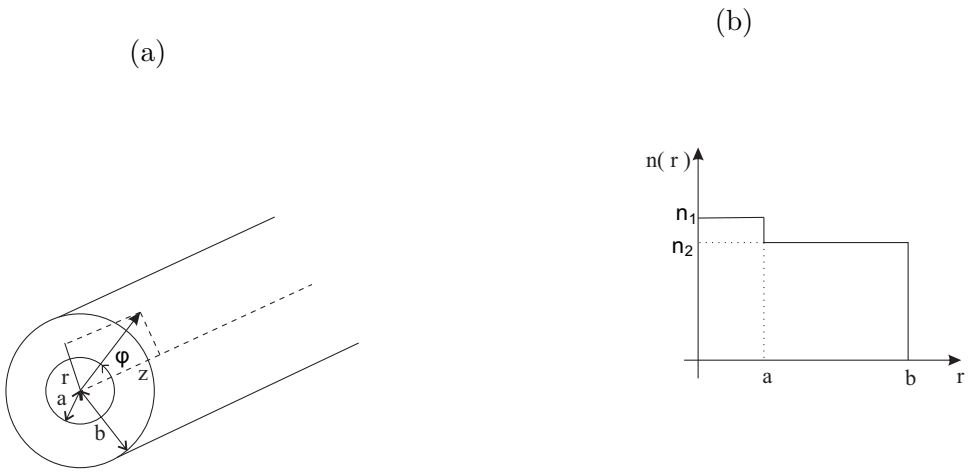

Figure 2.1: (a) Geometry and coordinate system of a step-index optical fiber (b) Profile of its refractive index as a function of r

for each of these two regions. The continuity of electric and magnetic fields at the core-cladding boundary helps to determine the unknown parameters in the solution. The steps are worked out in detail in [16, 17, 21]. The transcendental equation for the propagation constant β:

$$\left(\frac{J_l'(ha)}{haJ_l(ha)}+\frac{K_l'(qa)}{qaK_l(qa)}\right)\left(\frac{n_1^2J_l'(ha)}{haJ_l(ha)}+\frac{n_2^2K_l'(qa)}{qaK_l(qa)}\right)=\left(\frac{l\beta}{k_0}\right)^2\left[\left(\frac{1}{ha}\right)^2+\left(\frac{1}{qa}\right)^2\right], \quad (2.1)$$

where $J_l(x)$ and $J_l'(x)$ are the Bessel function of the first kind and its derivative respectively, $K_l(x)$ and $K_l'(x)$ are the modified Bessel function of the second kind and its derivative respectively, n_1 and n_2 are the refractive indices of core and cladding respectively, a is the radius of core, $l = 0, 1, 2, ...$ for different modes. The following quantities are introduced:

$$\begin{aligned} h &= \sqrt{n_1^2k_0^2-\beta^2} \\ q &= \sqrt{\beta^2-n_2^2k_0^2} \end{aligned} \quad (2.2)$$

The propagation constant β is defined such that the solution of the electric field is given by,

$$\vec{E} \propto \exp[-i(\beta z-\omega t)] \quad (2.3)$$

For any lossless modes to be confined to the core, β lies within the range $n_2 k_0 \leq \beta \leq n_1 k_0$, where $k_0 = \omega/c$ is the wave vector of the field in vacuum.

By solving Eq. (2.1) numerically, one obtains a discrete set of values for β, each of which corresponds to a different propagating mode in an optical fiber. If the mode has all six non-vanishing components (E_r, E_ϕ, E_z, H_r, H_ϕ, H_z in cylindrical coordinates) then it is called a hybrid mode (HE or EH). If it has no electric field in the direction of propagation ($E_z = 0$), then it is called transverse electric a (TE) mode. Similarly, if it has no magnetic field in the direction of propagation ($H_z = 0$), then it is called a transverse magnetic (TM) mode.

Re-arranging Eq. (2.1) and making use of relations

$$\begin{aligned} J_l'(x) &= J_{l-1}(x) - \frac{l}{x} J_l(x), \\ K_l'(x) &= -\frac{1}{2}[K_{l-1}(x) + K_{l+1}(x)] \end{aligned} \tag{2.4}$$

to obtain

$$\frac{J_{l-1}(ha)}{haJ_l(ha)} = \left(\frac{n_1^2 + n_2^2}{2n_1^2}\right) \frac{K_{l-1}(qa) + K_{l+1}(qa)}{2qaK_l(qa)} + \frac{l}{(ha)^2} \pm R \tag{2.5}$$

where

$$R = \left[\left(\frac{n_1^2 - n_2^2}{2n_1^2}\right)^2 \left(\frac{K_{l-1}(qa) + K_{l+1}(qa)}{2qaK_l(qa)}\right)^2 + \left(\frac{l\beta}{n_1 k_0}\right)^2 \left(\frac{1}{(qa)^2} + \frac{1}{(ha)^2}\right)^2\right]^{1/2} \tag{2.6}$$

The $\pm$ signs in Eq. (2.5) represent two different sets of hybrid modes, the HE(-) and EH(+). This designation stands on the contribution of E_z and H_z to the mode: E_z is larger (smaller) than H_z for the EH (HE) modes. For each set of modes there exist different solutions based on the value of l. These modes are labeled as EH_{lm} and HE_{lm} where m stands for the different solutions of Eq. (2.5) for a fixed l. There are two special cases with $l = 0$: TM modes, solutions for EH_{0m} and TE modes solutions for HE_{0m}. The different possible solutions of Eq. (2.5) are summarized in Table 2.1. It can be shown graphically, TE, TM and EH modes all have a cutoff diameter below which their corresponding fundamental modes cannot propagate. However, for HE modes there is no such cutoff value (or lower limit). It is useful

Modes	Sign	l value	Field components
HE	$-$	> 0	$E_z, E_r, E_\phi, H_z, H_r, H_\phi$
EH	$+$	> 0	$E_z, E_r, E_\phi, H_z, H_r, H_\phi$
TE	$-$	0	E_ϕ, H_z, H_r
TM	$+$	0	H_ϕ, E_z, E_r

Table 2.1: Modes propagating in the fiber with their field components and l values indicated. The 'sign' refers to the two branches in the solutions of Eq. (2.5)

to define the following fundamental V parameter for the fiber-field system.

$$V = \frac{2\pi a}{\lambda}\sqrt{n_1^2 - n_2^2} \tag{2.7}$$

Among TM, EH and TE modes, the TM modes have the lowest cutoff diameter value for its fundamental mode TM_{01} and it occurs at $V = 2.405$. Below this cutoff value only the fundamental mode (HE_{11}) can propagate. Therefore, the single mode condition for a given wavelength is given by,

$$V < 2.405 \tag{2.8}$$

Physically, as a mode approaches this cutoff value from above, the field penetrates deeper into the cladding. The mode is poorly confined in the core and a significant amount of energy propagates as evanescent field in the cladding. On the contrary, when far above cutoff, the mode is tightly confined to the core and most of the energy propagates as the guided mode.

2.2 Propagation of fundamental mode inside and outside of a nanofiber

In this section, the intensity distribution of the HE_{11} mode of an optical nanofiber and some related parameters for our tapered nanofiber will be explored. For our case, $n_1 = 1.453$, $n_2 = 1$ and $\lambda = 780.24$ nm (corresponding to D_2 transition of ^{87}Rb). The values of n_1 and n_2 are due to the fact that a nanofiber has a non-existent core and what remains is only the cladding.

2.2.1 Upper limit of the nanofiber diameter

For coherent interaction with atoms through the evanescent field of the nanofiber, the nanofiber should support single mode operation and strong confinement. It should satisfy Eq. (2.8) for the wavelength $\lambda = 780.24$ nm which implies,

$$2a < 566.62 \text{ nm} \tag{2.9}$$

where a is the radius of nanofiber. Therefore, it is imperative to fabricate nanofibers with diameter less than 566.62 nm. In Chapter 4, I will describe in detail the process of tapering the fiber down to this sub-micron diameter.

2.2.2 Field distribution of the HE_{11} mode: Quasi-linear polarization

I present here the field intensity distribution of the HE_{11} mode inside and outside of the nanofiber. A detailed discussion of nanofiber fundamental modes for circular and quasi-linear polarization can be found in [22, 34]. Let us consider a laser field (TEM_{00}), linearly polarized along the x-axis, being injected into the fiber. Although at the beginning of tapered region $E_x \neq 0$ and $E_y = E_z = 0$, the polarization structure of the field becomes complicated at the nanofiber region. The field has components along all three axes x, y, z and additionally the longitudinal field component E_z is $\pi/2$ phase-shifted compared to the other components. At this sub-wavelength light confinement regime, the field components E_x, E_y, E_z have amplitudes comparable to each other. The solution of the fields (with $x = r\cos\phi, y = r\sin\phi$) are:

For $r < a$,

$$
\begin{aligned}
E_x(r,\phi,z,t) &= A_{lin}\frac{\beta_{11}}{2h_{11}}\big[(1-s_{11})J_0(h_{11}r)\cos(\phi_0)- \\
&\qquad (1+s_{11})J_2(h_{11}r)\cos(2\phi-\phi_0)\big]\exp[i(\omega t-\beta_{11}z)], \\
E_y(r,\phi,z,t) &= A_{lin}\frac{\beta_{11}}{2h_{11}}\big[(1-s_{11})J_0(h_{11}r)\sin(\phi_0)- \\
&\qquad (1+s_{11})J_2(h_{11}r)\sin(2\phi-\phi_0)\big]\exp[i(\omega t-\beta_{11}z)], \\
E_z(r,\phi,z,t) &= iA_{lin}J_1(h_{11}r)\cos(\phi-\phi_0)\exp[i(\omega t-\beta_{11}z)]
\end{aligned} \tag{2.10}
$$

For $r > a$,

$$
\begin{aligned}
E_x(r,\phi,z,t) &= A_{lin}\frac{\beta_{11}}{2q_{11}}\frac{J_1(h_{11}a)}{K_1(q_{11}a)}\big[(1-s_{11})K_0(q_{11}r)\cos(\phi_0)+ \\
&\qquad (1+s_{11})K_2(q_{11}r)\cos(2\phi-\phi_0)\big]\exp[i(\omega t-\beta_{11}z)], \\
E_y(r,\phi,z,t) &= A_{lin}\frac{\beta_{11}}{2q_{11}}\big[(1-s_{11})K_0(q_{11}r)\sin(\phi_0)+ \\
&\qquad (1+s_{11})K_2(q_{11}r)\sin(2\phi-\phi_0)\big]\exp[i(\omega t-\beta_{11}z)], \\
E_z(r,\phi,z,t) &= iA_{lin}\frac{J_1(h_{11}a)}{K_1(q_{11}a)}K_1(q_{11}r)\cos(\phi-\phi_0)\exp[i(\omega t-\beta_{11}z)]
\end{aligned} \tag{2.11}
$$

where

$$
\begin{aligned}
h_{11} &= \sqrt{k_0^2n_1^2-\beta_{11}^2}, \\
q_{11} &= \sqrt{\beta_{11}^2-k_0^2n_2^2}, \\
s_{11} &= \left[\frac{1}{(h_{11}a)^2}+\frac{1}{(q_{11}a)^2}\right]\left[\frac{J_1'(h_{11}a)}{h_{11}aJ_1(h_{11}a)}+\frac{K_1'(q_{11}a)}{q_{11}aK_1(q_{11}a)}\right]^{-1}
\end{aligned} \tag{2.12}
$$

A_{lin} is the real-valued normalization constant for the linearly polarized input and is given by,

$$
A_{lin} = \sqrt{2}\left(\frac{4\mu_0\omega P}{\pi a^2\beta_{11}}\right)^{1/2}(D_{in}+D_{out})^{-1/2}, \tag{2.13}
$$

with

$$D_{in} = \big[(1-s_{11})(1+(1-s_{11})\frac{\beta_{11}^2}{h_{11}^2})(J_0^2(h_{11}a)+J_1^2(h_{11}a)+ \\ (1+s_{11})(1+(1+s_{11})\frac{\beta_{11}^2}{h_{11}^2})(J_2^2(h_{11}a)-J_1(h_{11}a)J_3(h_{11}a))\big], \tag{2.14}$$

$$D_{out} = \frac{J_1^2(h_{11}a)}{K_1^2(q_{11}a)}\big[(1-s_{11})(1-(1-s_{11})\frac{\beta_{11}^2}{q_{11}^2})(K_0^2(q_{11}a)+K_1^2(q_{11}a)+ \\ (1+s_{11})(1-(1+s_{11})\frac{\beta_{11}^2}{q_{11}^2})(K_2^2(q_{11}a)-K_1(q_{11}a)K_3(q_{11}a))\big]. \tag{2.15}$$

where $D_{in}/(D_{in}+D_{out})$ and $D_{out}/(D_{in}+D_{out})$ are the fractions of the power of the fields propagating inside and outside of the nanofiber respectively, $\omega = 2\pi c/\lambda$, and P is the total power transmitted through the nanofiber and can be measured directly at the fiber output. Also, P can be related to Poynting vector as following:

$$P = \int_0^{2\pi} d\phi \int_0^a \langle S_z \rangle r dr, \tag{2.16}$$

where $\langle S_z \rangle$ is the z-component of the cycle-averaged Poynting vector $\langle \vec{S} \rangle = \frac{1}{2} Re\Big[\vec{E} \times \vec{H}\Big]$, which is a measure of the energy flux of the electromagnetic field in the propagation direction. The squared modulus of the electric field averaged over one oscillation period in the HE_{11} mode inside (in) and outside (out) of the nanofiber is given by,

$$|\vec{E}(r,\phi)|_{in}^2 = \frac{A_{lin}^2\beta_{11}^2}{4h_{11}^2}\Bigg[(1-s_{11})^2J_0^2(h_{11}r)+(1+s_{11})^2J_2^2(h_{11}r)+2\frac{h_{11}^2}{\beta_{11}^2}J_1^2(h_{11}r) \\ +2\left(\frac{h_{11}^2}{\beta_{11}^2}J_1^2(h_{11}r)-(1+s_{11})(1-s_{11})J_0(h_{11}r)J_2(h_{11}r)\right)\cos[2(\phi-\phi_0)]\Bigg] \tag{2.17}$$

$$|\vec{E}(r,\phi)|_{out}^2 = \frac{A_{lin}^2\beta_{11}^2J_1^2(h_{11}a)}{4q_{11}^2K_1^2(q_{11}a)}\Bigg[(1-s_{11})^2K_0^2(q_{11}r)+(1+s_{11})^2K_2^2(q_{11}r)+2\frac{q_{11}^2}{\beta_{11}^2}K_1^2(q_{11}r) \\ +2\left(\frac{q_{11}^2}{\beta_{11}^2}K_1^2(q_{11}r)-(1+s_{11})(1-s_{11})K_0(q_{11}r)K_2(q_{11}r)\right)\cos[2(\phi-\phi_0)]\Bigg] \tag{2.18}$$

In Fig. 2.2, field intensity distribution of the electric field is plotted as a function of cartesian components x, y, z such that $|\vec{E}|^2 = |\vec{E}_x(r,\phi,z)|^2 + |\vec{E}_y(r,\phi,z)|^2 + |\vec{E}_z(r,\phi,z)|^2$.

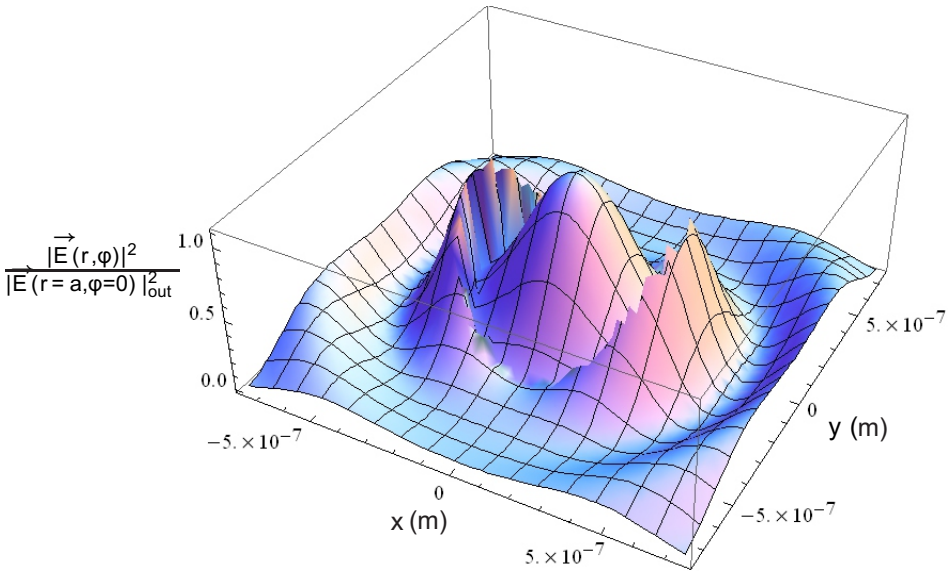

Figure 2.2: $|\vec{E}(r,\phi)|^2$ normalized to $|\vec{E}(r=a,\phi=0)|^2_{out}$ is plotted against x and y axes (where z is the field propagation direction) for a nanofiber of radius $a = 350$ nm.

Due to the large difference in refractive index at the boundary between cladding and vacuum (or air) there is a discontinuity in the normal component E_r of the field, which causes a jump in intensity leading to an enhancement of the evanescent field strength outside the nanofiber. The term $\cos[2(\phi - \phi_0)]$ in Eqns. (2.17) and (2.18) breaks the spatial azimuthal symmetry of the system such that the maximum intensity of the evanescent field occurs at $\phi = 0$ and the minimum at $\phi = \pi/2$. With x-polarized electric field injected into the nanofiber, the evanescent field strength along x is expected to remain the strongest, even though there are non-zero contributions to the field energy from y and z components, at the tapered region. The maximum of the evanescent field intensity distribution at the nanofiber surface occurring at $\phi = 0$ (i.e. along x direction) (shown in Fig. 2.3) supports our intuition.

The decay length (length at which the field intensity drops to $1/e$ of its value at the nanofiber surface) of the evanescent field is defined by $\Lambda_{11} = 1/q_{11}$. It is polarization independent and scales with the wavelength of light. For $\lambda = 780.24$ nm, propagation constant for fundamental mode i.e. β_{11} can be found by solving Eq. (2.1) and hence the decay length

(a)

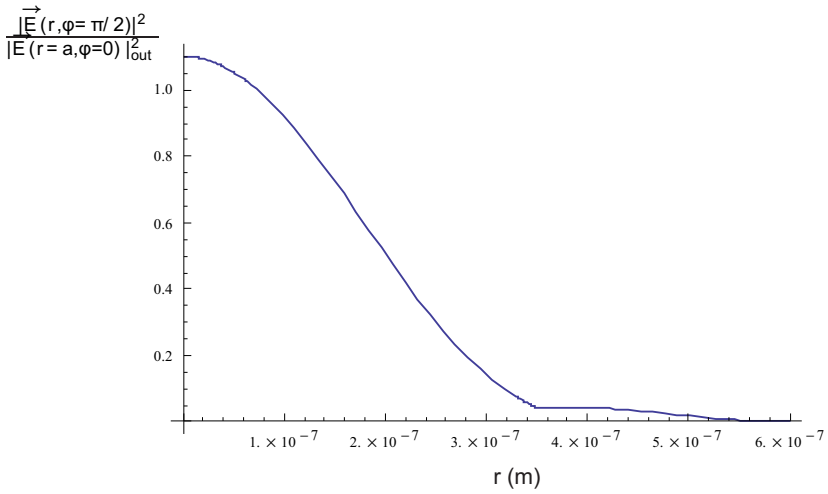

(b)

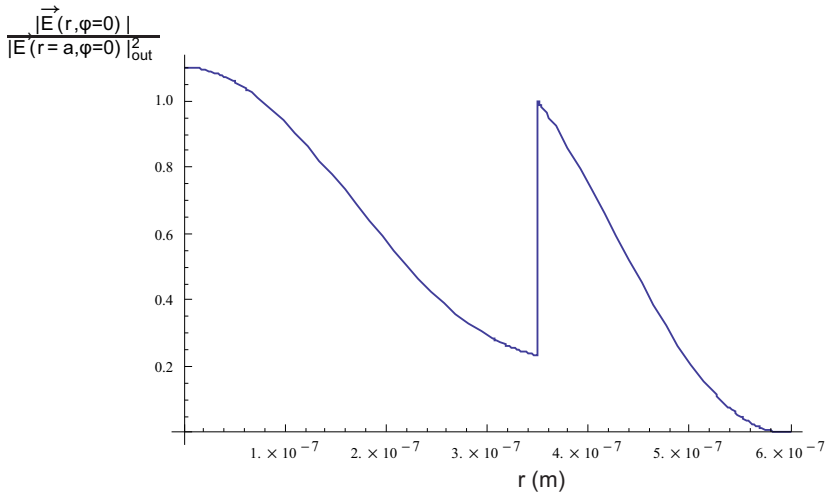

Figure 2.3: $|\vec{E}(r,\phi)|^2$ normalized to $|\vec{E}(r=a,\phi=0)|^2_{out}$ plotted as a function of r, for a nanofiber of radius $a = 350$ nm, at (a) $\phi = \pi/2$ and (b) $\phi = 0$

is calculated by using Eq. (2.12)

$$\beta_{11} = 1.238\ \mu m^{-1}$$
$$\Lambda_{11} = \frac{1}{\sqrt{\beta_{11}^2 - k_0^2 n_2^2}} = 170.067\ \text{nm} \tag{2.19}$$

with $n_2 = 1$ and $k_0 = 8.053\ \mu m^{-1}$ for $\lambda = 780.246$ nm.

A question that naturally arises is - how does the evanescent field intensity of nanofiber varies with the diameter of nanofiber. It can be shown [17, 24] that the maximum intensity of the evanescent field at the surface of the nanofiber is reached when $a/\lambda = 0.23$ i.e. $|\vec{E}(x = a, y = 0)|^2_{out}$ has a maximum value for $a = 0.23\lambda$ when the x-polarized electric field is injected into the nanofiber. A further reduction of the diameter leads to a poor radial confinement of the field and ultimately at some smaller diameter, the fiber will not be able to transmit any light through it (a drastic increase of the mode diameter transforming $\vec{E}$ into a plane wave for vanishing radius). This result holds universally for all wavelengths (in the visible and near-infrared region) as long as the silica fibers are used.

For our case $\lambda = 780.24$ nm, the optimal value for $a/\lambda = 0.23$ occurs at $2a = 359$ nm. Thus, the thickness of our nanofibers should be less than 566.62 nm (to satisfy the single-mode criterion Sec. 2.2.1) and close to the optimal value of 359 nm for best possible results in the experiment. In reality, we do routinely fabricate nanofibers in this optimal regime, with diameters between 300 and 400 nm.

Chapter 3

Magneto-optical trap (MOT)

The most popular and widely used trap for neutral atoms, employing both optical and magnetic fields is magneto-optical trap (MOT). The principal idea of magneto-optical trapping was suggested by Jean Dalibard and demonstrated at Bell Laboratories, USA in collaboration with a group from MIT in 1987 [42]. The MOT combines both inhomogeneous magnetic fields and radiative selection rules to make use of both optical pumping and strong radiative force to trap atoms.

In this chapter, some of the principles behind MOT are briefly discussed. For a detailed discussion on laser cooling and trapping, the reader is referred to [18, 15].

3.1 Laser cooling

The atoms are in continuous motion and they do not see the laser beam at the same frequency as in the laboratory frame of reference. The laser frequency will be shifted for a moving atom by $\vec{k} \cdot \vec{v}$ due to the Doppler effect. If a laser beam, with frequency ω and wave-vector $\vec{k}$, is propagating in a direction opposite to that of an atom, having velocity $\vec{v}$ then $\omega_A = \omega - \vec{k} \cdot \vec{v} = \omega + kv$ (since $\vec{v}$ points opposite to $\vec{k}$) is the frequency in the atomic frame. When this frequency is equal to the atomic transition frequency ω_0 , i.e. $\omega_A = \omega_0$ then the atom will absorb the photon and it will get a momentum kick, due to momentum conservation, in a direction opposite to its motion. After absorbing the photon the atom is in the excited state and will spontaneously emit photons to return to the ground state. These photons are emitted in all directions from the atom such that on average zero force is imparted on the atom. Thus, the scattering of many photons gives an average force that slows down the atom. The magnitude of this scattering force on the atom can be calculated

as follows:

$$F_{scat} = (\text{Rate of scattering}) \times (\text{Momentum imparted by absorbing a photon})$$

Now in the steady state, the scattering rate R_{scat} should be equal to the rate at which photons are spontaneously emitted from the atomic ensemble, the latter being equal to decay rate of transition Γ times the fraction of population in the excited state ρ_{ee}.

$$\begin{aligned} R_{scat} &= \Gamma\rho_{ee} \\ &= \frac{\Gamma}{2}\frac{\Omega^2/2}{\Delta^2 + (\Gamma/2)^2 + \Omega^2/2} \end{aligned} \tag{3.1}$$

where $\Omega = d\mathcal{E}_0/\hbar$ is the Rabi frequency, $\Delta = \omega - \omega_0 - \vec{k}\cdot\vec{v}$ is the frequency detuning between the laser frequency ω and the atomic resonance frequency ω_0, taking into account the Doppler shift $\vec{k}\cdot\vec{v}$. With photons having momentum $\hbar k$, the scattering force is given by,

$$F_{scat}(\Delta) = \hbar k\frac{\Gamma}{2}\frac{\Omega^2/2}{\Delta^2 + (\Gamma/2)^2 + \Omega^2/2} \tag{3.2}$$

As $\Omega \to \infty$, the force tends to a limiting value given by $F_{max} = \hbar k\Gamma/2$ ($\Gamma/2$ is the rate of spontaneous emission in a two-level atomic system at high intensities as the population in both ground and excited states approach 1/2).

This radiation force will result in deceleration of the atom and its maximum value is given by,

$$a_{max} = \frac{F_{max}}{M} = \frac{\hbar k\Gamma}{2M} = \frac{v_r}{2\tau} \tag{3.3}$$

where $v_r = \frac{\hbar k}{M}$ is the recoil velocity, τ is the lifetime of the excited state and M is the mass of the atom. Typically, $v_r \approx$ few cm/s and excited state lifetimes, $\tau \approx$ tens of ns, such that the maximum deceleration experienced by the atom is $a_{max} \approx 10^5 - 10^6$ ms^{-2}, which is at least four orders of magnitude larger than gravitational acceleration.

Optical molasses is the name given to the laser cooling technique that uses three orthogonal pairs of counter-propagating laser beams to damp the atomic motion. The laser beams

are derived from the same laser having a frequency ω, which is slightly red-detuned from the resonance frequency. With the laser slightly detuned below resonance, atoms moving toward one beam see it Doppler shifted upward, closer to resonance. Since such atoms are moving away from the other beam, they see it Doppler shifted further downward, hence further out of resonance. Atoms therefore scatter more light from the beam counter-propagating to their velocity, and their velocity is lowered. A stationary atom in a pair of counter-propagating laser beams experiences no force because the scattering of light is the same for both beams. Due to counter-propagating beams in x, y and z directions, all the atoms in the ensemble are slowed down based due to the damping mechanism. More discussions including the dependency of the damping force on the atomic velocity will be found in next section Sec. 3.2.

3.2 MOT

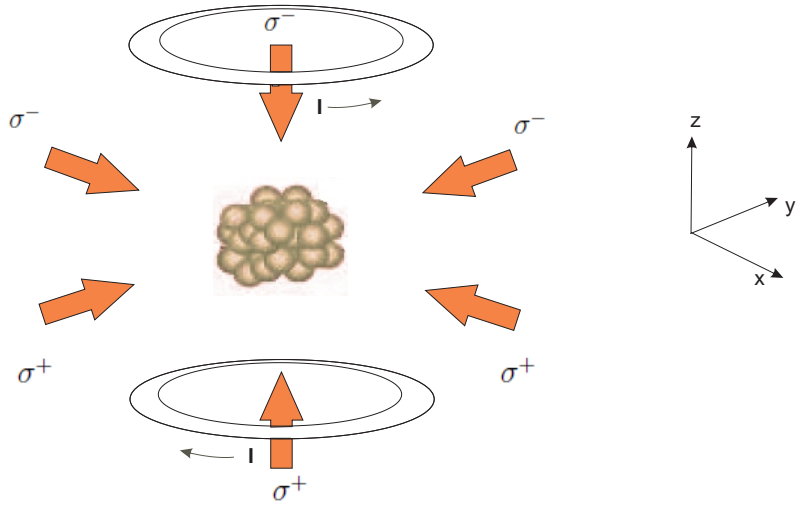

Figure 3.1: Schematic of magneto-optical trap

In order to trap a large ensemble of atoms, the atoms need not only be cooled but also confined to a specific region of space. The MOT requires three orthogonal pairs of counter-propagating red-detuned laser beams. Each pair is comprised of one σ^+ and one σ^- field (e.g., two right-circularly polarized counter-propagating laser fields). In addition, a uniform magnetic field gradient about the center is created by a pair of coils in anti-Helmholtz configuration (i.e., the current in the two coils circulate in opposite directions with respect to each other) as shown in Fig. 3.1. A MOT is typically formed with a pair of counter-propagating right-circularly beams along the z-axis and two pairs of counter-propagating left-circularly polarized beams along the x- and y- axes. The right- and left-circular polarizations in practice, may have to be swapped based on the $\vec{B}$ field direction, but the important point to note is two pairs of beams in the x-y plane have one polarization while the beam pair along z have the other polarization. This is because the sense of direction of $\vec{B}$ field lines along x and y are opposite to that of z such that their field gradients are related by

$$\frac{\mathrm{d}B_x}{\mathrm{d}x} = \frac{\mathrm{d}B_y}{\mathrm{d}y} = -\frac{1}{2}\frac{\mathrm{d}B_z}{\mathrm{d}z} \tag{3.4}$$

The magnetic field at the center of the coils cancel out ($B = 0$). This field gradient about the center causes Zeeman splitting of atomic energy levels. The principle of MOT is illustrated in Fig. 3.2 for a hypothetical atomic transition $F = 0$ to $F = 1$. Now, because of the magnetic field gradient the Zeeman effect causes the energy of the three sub-levels (with $m_F = 0, \pm 1$) to vary linearly with position of atom along z-axis.

Consider an atom moved from the center of the trap along the z-axis with $z > 0$, so that $\Delta m_F = -1$ transition comes closer to resonance with the laser frequency, which is slightly red-detuned to the atomic resonance. It's a combination of Doppler effect and the Zeeman shift, obeying the selection rules, that leads to absorption of photons from the σ^- beam propagating in -z direction. This excites the transition $F = 0$, $m_F = 0 \rightarrow F = 1$, $m_F = -1$ that provides a scattering force which is stronger than the force generated by the scattering

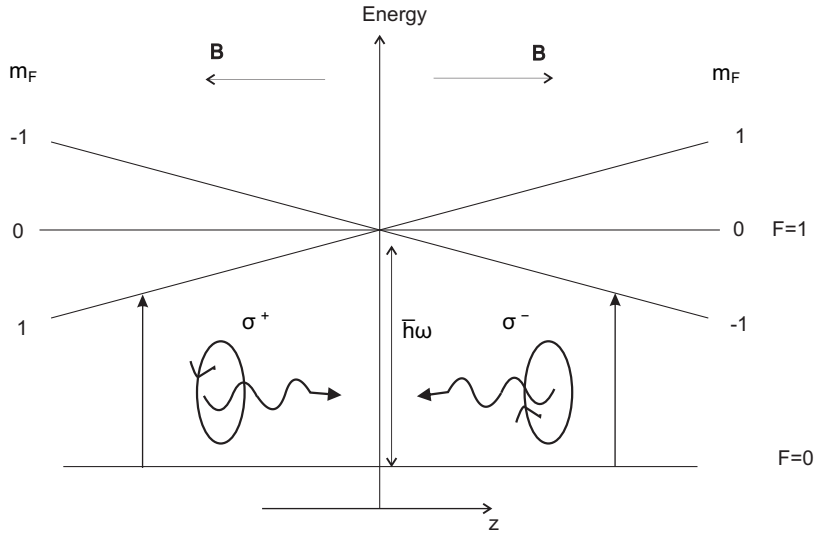

Figure 3.2: Conceptual schematic for a one-dimensional trap, which is extended to 3 dimensions in MOT

of photons from the σ^- beam propagating in $+z$-direction. The net force pushes the atom back towards $z = 0$. A similar mechanism occurs for another atom at $z < 0$. In this case, Zeeman shift as well as Doppler effect favors absorption of photons from the beam (σ^+) propagating in the $+z$ direction, that pushes the atom back towards the same trap center $z = 0$.

To have quantitative expressions for the scattering force on atoms in a MOT, let us investigate how the presence of magnetic field shifts the magnetic sublevels. The states concerned are the magnetic sublevels m_F of the same hyperfine level F. Because of the anti-Helmholtz coils, the first order energy shift to the magnetic sublevel m_F is $\Delta E_{F,m_F} = \mu_B g_F m_F B_z$ [43] as calculated from time-independent perturbation theory where Bohr magneton $\mu_B = e\hbar/2m_{electron}$ and Lande g-factor g_F, whose values can be found in Ref. [45]. Since the magnetic field changes linearly in space around the zero-field point, for small displacements we can write: $B_z = \frac{\partial B_z}{\partial z} z$. For a transition between two levels, both levels are

shifted by the magnetic field. Therefore, the net energy shift for a particular transition,

$$\Delta E_{F',m_{F'}} - \Delta E_{F,m_F} = (g_{F'} m_{F'} - g_F m_F)\mu_B \frac{\partial B_z}{\partial z} z \tag{3.5}$$

For our scheme in Fig. 3.2, $F = 0$, $m_F = 0$, $F' = 1$, $m_{F'} = 0, \pm 1$ (depending on z). Thus, we can write the frequency shift as,

$$\Delta\omega = m_{F'} \frac{g_{F'}\mu_B}{\hbar} \frac{\partial B_z}{\partial z} z = m_{F'}\beta z \tag{3.6}$$

(since $m_F = 0$ implying $g_{F'}$ same for all $m_{F'}$ [45]).

$$\beta = \frac{g_{F'}\mu_B}{\hbar} \frac{\partial B_z}{\partial z} \tag{3.7}$$

Now we can account for the detuning caused by both Doppler effect and Zeeman shift. The net detuning is $\Delta = \omega - \omega_0 - \vec{k} \cdot \vec{v} - m_{F'}\beta z$ where ω is the laser frequency and ω_0 is the atomic resonance frequency. For a pair of counter-propagating beams $\sigma^{\pm}$, $\vec{k}_{\pm}$ signify the beam propagation direction such that $\vec{k}_- = -\vec{k}_+$ and $|\vec{k}_-| = |\vec{k}_+| = k$. The atom with velocity $\vec{v}$ will come into resonance with σ^- beam (having wave-vector $-\vec{k}$) which will address the transition to $m_F = -1$ level for $+z$ position. The detuning in this case for σ^- beam is $\Delta_{\sigma^-} = \omega - \omega_0 + kv + \beta z$. For the same atom, the detuning is $\Delta_{\sigma^+} = \omega - \omega_0 - kv - \beta z$ when addressed by σ^+ beam. Therefore, the net scattering force experienced by the atom, with the help of Eq. (3.2), has the form:

$$\begin{aligned} F_{MOT} &= F_{scat}(\Delta_{\sigma^+}) - F_{scat}(\Delta_{\sigma^-}) \\ &= F_{scat}(\omega - \omega_0 - kv - \beta z) - F_{scat}(\omega - \omega_0 + kv + \beta z) \\ &\simeq -2\frac{\partial F_{scat}}{\partial \omega} kv + 2\frac{\partial F_{scat}}{\partial \omega_0}\beta z \end{aligned} \tag{3.8}$$

where we expand up to first order in Taylor's series expansion since $\beta z \ll \omega_0$ and $kv \ll \omega$. Differentiation of Eq. (3.2) with respect to ω gives the damping coefficient defined as

$$\alpha = 2k\frac{\partial F_{scat}}{\partial \omega} = \frac{8\hbar k^2 \Omega^2}{\Gamma^2} \frac{-2(\omega - \omega_0)/\Gamma}{[1 + (2(\omega - \omega_0)/\Gamma)^2]^2} \tag{3.9}$$

With $\frac{\partial F}{\partial \omega} = -\frac{\partial F}{\partial \omega_0}$ we finally have,

$$F_{MOT} = -\alpha v - \frac{\alpha\beta}{k} z \tag{3.10}$$

where α and β are defined by Eq. (3.7) and Eq. (3.9) respectively.
The frictional term $-\alpha v$ damps the atomic motion while the harmonic term $\alpha\beta/k$ traps the atom. In a nutshell, the atom undergoes over-damped simple harmonic motion. The positivity of α is ensured by the detuning of the laser (commonly called cooling or trapping laser) below resonance. The optimal value of this red detuning, found by maximizing α, is $\omega - \omega_0 = -\frac{\Gamma}{2\sqrt{3}}$. Substituting the value of decay rate Γ for ^{87}Rb (from Table. 5.1), the optimal detuning is -11 MHz. The detuning used in the experiment is -9 MHz, which is close to the optimum.

MOT is a robust trap that does not depend on precise balancing of the counter-propagating beams or on a very high degree of polarization. The trapping is a dynamic process such that there are always atoms leaving and entering the MOT. Hence, there has to be a constant supply of atoms to replenish the ones that are leaving the trap.

For real atoms, the hyperfine levels are labeled by $\hat{\mathbf{F}} = \hat{\mathbf{I}} + \hat{\mathbf{J}}$ where $\hat{\mathbf{J}}$ is the electron's total angular momentum and $\hat{\mathbf{I}}$ is the nuclear spin angular momentum. For the D_2 transition of ^{87}Rb, there are two hyperfine ground levels $F = 1$ and $F = 2$. The cooling transition is chosen to be $F = 2 \rightarrow F' = 3$ with most of the atoms decaying back to $F = 2$ (since it is a cyclic transition) so that the atoms can be addressed by the cooling laser for many consecutive cycles. However, a portion of atoms decays back into the dark state $F = 1$ (for new atoms they have a non-zero, finite probability to be in $F = 1$ as they enter the trap). These atoms will not be confined anymore and can escape the trap. To keep the atoms in the trap, another laser field called the repumping laser accompanies the cooling laser to excite the atoms from $F = 1 \rightarrow F' = 2$ and let them decay back to $F = 2$ where they can be laser-cooled and trapped.

The atoms in a MOT get heated up partly due to the random spontaneous emission from

the trapped atoms in three dimensions and partly due to the fluctuations in the number of photons absorbed by the atoms [15]. The competing heating and cooling processes lead to an equilibrium temperature, **Doppler limit temperature** for a steady state MOT and is given by,

$$T_D = \frac{\hbar\Gamma}{2k_B} \tag{3.11}$$

where k_B is the Boltzmann constant. For ^{87}Rb $T_D = 146$ μK. However, the temperature in optical molasses was experimentally found much lower than predicted. It was then understood that there are other cooling mechanisms in operation resulting from an interplay between spin and external degrees of freedom and between dissipative and dispersive effects, explored in Sisyphus cooling and polarization gradient cooling techniques [18].

3.3 MOT regimes and some parameters

There are four distinct regimes for a steady-state MOT cloud. The simplest way to picture the cloud's transition between different regimes is to keep the trapping conditions same while looking at changing the number of atoms trapped. The regimes are as follows:

1. The temperature limited regime is the regime where the MOT cloud has the least number of atoms. The trapping force is same as that calculated in the previous section. Assuming spherical symmetry, $F(r, v_r) = -\alpha v_r - \kappa r$. The size of the cloud depends only on the temperature and not on the number of the atoms. Hence, the atomic density is proportional to the number of trapped atoms as long as the spring constant κ remains unchanged.

2. The multiple scattering regime is where the atomic cloud has become dense enough so that a major portion of the fluorescence photons are re-absorbed by the atoms in the cloud. This re-scattering results in a repulsive force between the atoms, which limits the density of the cloud in this regime. The size of

the cloud is no longer determined by the cloud temperature but rather by the number of trapped atoms because of the repulsive forces between atoms at higher densities. The density in this regime no longer depends on the number of atoms but only on the spring constant κ and trap intensity.

3. The two-component regime is where the number of atoms is too high to fit into the harmonic trap and as a result atoms spill out of the trap into a shallower potential well around the harmonic trap. The approximation of the trap as a damped harmonic oscillator is no longer valid. The cloud appears to have a denser part within the harmonic trap with the density being much lower in the shallower region around the trap.

4. The optically dense or thick regime is where the shallower part of the trap is filled with atoms. This regime has the highest number of trapped atoms of the four regimes.

A MOT cloud is generally reported to be either in temperature limited regime or multiple scattering regime and hence the other two regimes are usually disregarded.

I will talk about the range for some of the parameters of a typical MOT reported by research groups worldwide. The cloud radius is on the order of few hundred microns to a few centimeters for the case of large laser beams. The cloud density is usually $10^9 - 10^{10}$ cm^{-3} and it can go up to to 10^{11} cm^{-3} for compressed magneto-optical trap (achieved by increasing the magnetic field gradient). The number of trapped atoms can vary from 10^6 to 10^9 depending on other parameters like the size of the MOT, the atomic density and the beam size.

Chapter 4

Tapered optical nanofiber (TNF)

A tapered optical nanofiber is fabricated by flame-pulling of a regular commercial fiber. Typically there are three different propagating zones (shown in Fig. 4.1) associated with a tapered nanofiber (also referred to as taper).

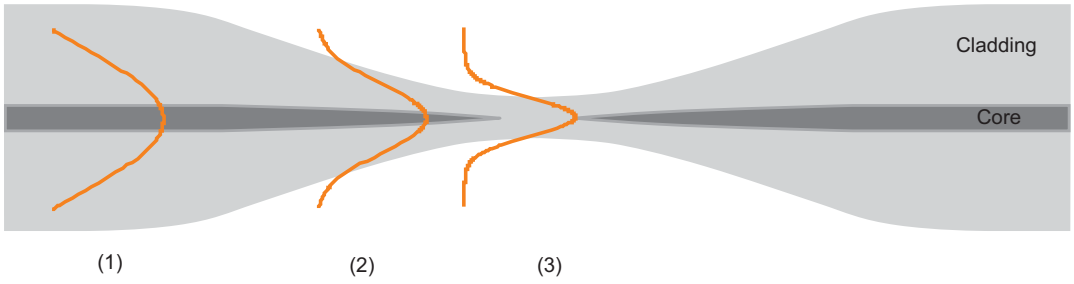

Figure 4.1: Schematic of light propagation in a tapered nanofiber (TNF) with labels (1)-(3) denoting the different propagation regions

(1) Unstretched single mode fiber: We have core-cladding guided mode in this region, with mode diameter of the order of several microns. Approximate solutions of Maxwell's equations can be found in this region, leading to linearly polarized modes.

(2) Taper transition: Here the fiber gets gradually thinner and so does the core. The field is compressed radially until the core becomes too thin to be able to guide the field. At this point, the light is guided in three regions: the unexpended core, the cladding and the surrounding air or vacuum. Finally, the fiber radius reduces down to the value at the taper waist (see the next

zone) thereby compressing the light field further. This compression should be ideally adiabatic [24] i.e. there should be no coupling between different higher modes and no coupling to the radiation modes in the process. The overall transmission of fiber decreases if there are uncontrolled mode excitations taking place in the taper transition region. The optimization of parameters for fiber-pulling process are of paramount importance to obtain something close to an adiabatic taper transition. The length of taper transition region for our nanofibers are typically: $L_z = 2 - 3$ cm.

(3) Taper waist: Here the fiber radius remains fairly constant at the subwavelength regime. We have cladding-air guided mode, which has a strong radial confinement and significant amount of energy propagates as evanescent wave outside the fiber taper. The lengths of the taper waist for our nanofibers are typically: $L_w = 1 - 2$ mm

The specifications of the single mode fiber, which we use for our experiment, are given by Table 4.1

Company, Part number	OZ Optics SMF-633-4/125-0.25-NF-L
Operating Wavelength	600-850 nm
Core Diameter	4μm
Cladding Diameter	125$\pm$2μm
Jacket Diameter	0.25 mm
Numerical Aperture	0.10-0.13
Cladding refractive index	1.453 @ 780.24 nm

Table 4.1: Single-mode fiber parameters and dimensions with cutoff at 600 nm

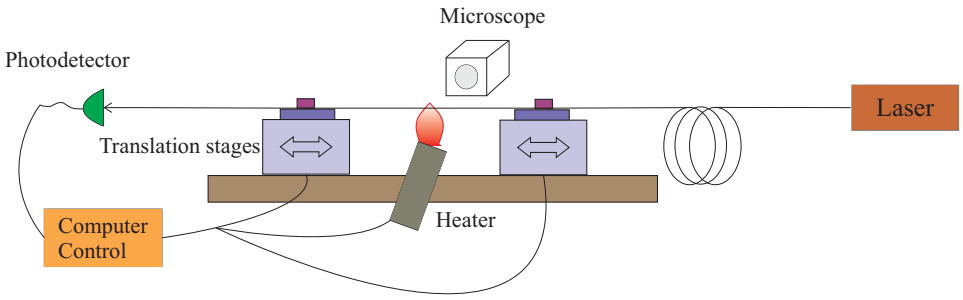

Figure 4.2: Schematic of fiber-pulling rig. A standard optical fiber is clamped between two translation stages which move and stretch the fiber above the flame of a heater. The pulling procedure is performed inside a closed environment.

4.1 Fabrication of a tapered nanofiber

4.1.1 Fiber-pulling setup

For fabrication of tapered nanofibers, we were priveleged to use the facilities in Prof. Paul Barclay's nanophotonics lab. The schematic of the fiber pulling rig is shown in Fig. 4.2. There are two main components, namely a heater (in our case a hydrogen flame torch) and a set of motorized fiber-pulling stages that can pull both ends of a standard optical fiber as it is being heated. The torch assembly consists of a torch (National Torches Model 3H Hydrogen Torch) and a 'hush' torch tip (National Torch Tips HT series). The two motorized translational stages (Suruga KXL06050-C1-C) are controlled by a stepping motor controller (Suruga DS102MS). The movements of torch and translation stages are controlled by Labview code. I will go on to describe the steps involved in this process.

- The polymer-coated jacket of the fiber (specifications in Table 4.1) is removed

with a fiber stripper for a length of around 10 cm. Also, one of the ends of the fiber is stripped and cut by a fiber cleaver (Ericsson EFC 11). This end is connected to a photodetector (New Focus Model 1621). A laser ($\lambda = 780$ nm) is injected into the fiber and the transmission is monitored in real-time.

- The stripped part of the fiber (referred to as bare fiber) is thoroughly cleaned by wiping it with isopropyl alcohol (IPA). The bare fiber is then mounted onto the fiber-pulling stages and fixed by a set of rotating fiber clamp (Thorlabs HFR007) to ensure a straight, torsionless mounting with a slight tension.

- The bare fiber is viewed in the microscope (positioned horizontally) and sometimes if there is still dust present then the last step is repeated.

- The hydrogen valve is opened and the torch is lit. Then a computer button is pressed to bring the heater in to the proximity of bare fiber such that fiber is placed in the upper edge of the flame (as shown in Fig. 4.3). The flow rates are adjusted to reach a temperature slightly above the softening point (1585°C for fused silica) and that allows taper pulling with minimal force. The optimal flow rate has been empirically found to be 290-300 mL/min (measured by the flow-meter).

- The fiber pulling is started immediately after the desired position of the heater is reached. The two motorized stages pull the fiber from both ends at speed 40μm/s, which is empirically found to be the optimal value for best fiber-pull. Both the profile of the bare fiber (seen through the microscope) and the transmission through the fiber is monitored during the process.

- Due to the change in the spatial geometry of the fiber in the process of fiber-pulling the fiber loses its single mode guiding properties slowly and becomes multimode. The interferences occurring between different modes of the

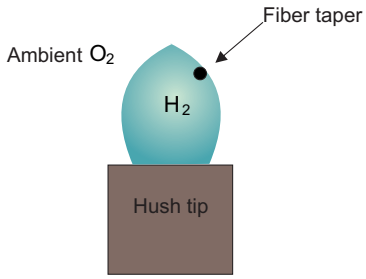

Figure 4.3: Schematic drawing of the optimal position of the fiber taper inside the hydrogen torch flame

fiber are manifested in the oscillations observed in the transmission profile in Fig. 4.4. There is a point where these oscillations stop and fiber becomes single mode ($V < 2.415 \Rightarrow 2a < 566$ nm discussed in Chapter 2) again. After reaching this point the pulling is stopped soon after. The whole fiber-tapering process takes about $3 - 5$ minutes.

- After the fiber-pulling, one can see the tapered fiber, mostly dangling or loose, in the microscope. Hence, the taper is re-tensioned (i.e. increased by small steps) using the motorized stages. This usually helps to improve the transmission marginally. We routinely fabricate nanofibers in the lab with a transmission of $90 - 95\%$.

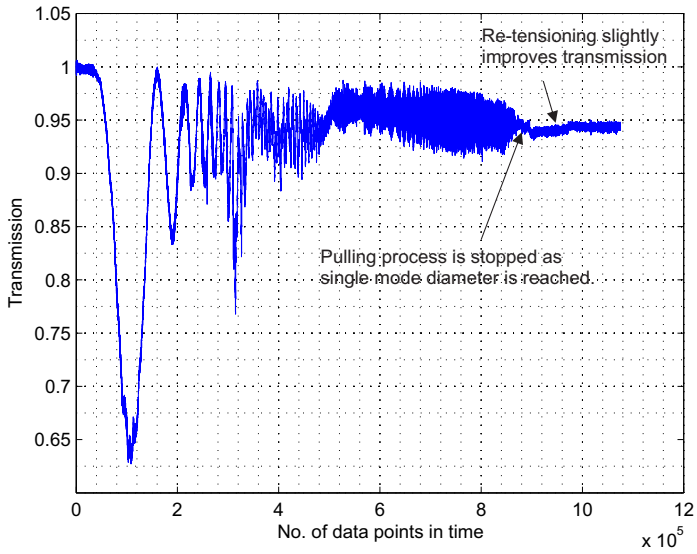

Figure 4.4: Transmission through a single-mode fiber as it is tapered down to a sub-micron diameter during a fiber-pull.

4.2 Transfer and manipulation of tapered nanofiber

A fiber taper is usually delicate and fragile, even more so at sub-wavelength diameter and hence a lot of planning, hard work have to be put in to keep it 'alive'. The taper will break if there is any small jerk or tension to the fiber. Additionally in our case, the nanofiber has to be transported from Prof. Barclay's lab to our lab. A series of steps are carried out systematically to extract the tapered nanofiber from the fiber pulling rig and insert it into the vacuum chamber.

4.2.1 Design of the taper mount

The taper mount, which we refer to as 'bracket' (marked in Fig. 4.5a) is made of stainless steel and was manufactured by the scientific workshop at U of C. The dimensions of the bracket are such that it can go in from below the taper and will gently touch the fiber taper

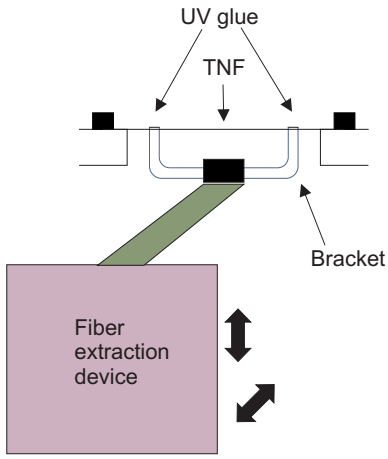

(a)

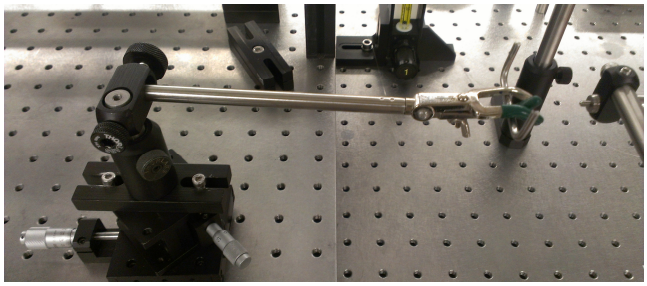

(b)

Figure 4.5: (a) Schematic of the extraction of nanofiber from the pulling rig onto the bracket (b) picture of the fiber extraction device

at two points. Also, it is designed in such a way so as not to block any portion of the six MOT beams inside the vacuum chamber.

4.2.2 Fiber extraction device

I have designed a special device for extraction of tapered nanofiber from the fiber-pulling setup. As shown in Fig. 4.5b , the device consists of a chemistry lab clamp mounted on vertical and horizontal translation stages. The clamp is used for holding the bracket and the whole device can be fixed to the optical table. The translation stages are used to bring the bracket close to the nanofiber and is brought from below, then slowly moved up until the fiber is inside the grooves of the bracket as shown in Fig. 4.5a.

Then, drops of glue (Dymax OP-4-20632) are put at the contact grooves of the bracket

and cured with UV lamp (Dymax BlueWave 75 UV Curing Spot Lamp with Intensity Adjustment). This glues the fiber taper onto the bracket. The transmission is monitored throughout the process and if there is any sudden drop in transmission, this implies the taper is damaged or broken.

4.2.3 UHV feed-through for nanofiber

The bracket-with-nanofiber is carefully removed from the fiber extraction device and attached to the arm of a gimbal mount. The fiber is fed through the holes of teflon ferrule and the ferrule is tightened by a nut in the Swagelok fitting [37]. The bracket holding the nanofiber is attached to an arm, which is attached to the gimbal mount (Fig. 4.6a). The two micrometer screws on the gimbal mount allow vertical and horizontal adjustment of position of the bracket in UHV. Fig. 4.6b shows the picture of a nanofiber securely installed in our fiber feed-through system. As shown, a lid like cover (made of acrylics which attracts dust particles) is put on the gimbal mount to protect the nanofiber from the surrounding dust. In fact, the nanofiber is secured in the above manner right after its fabrication and extraction. Then, it is transferred to our lab.

Any unwanted pressure to the hanging fiber or bracket can break the fiber from the edges of the bracket. This is equivalent to losing the nanofiber, because it is impossible to splice the short remaining part of fiber. So, each step is carried out with utmost care and precaution.

After the nanofiber is brought to our lab, its transmission is checked. The fiber ends are spliced with a fiber fusion splicer (Ericsson FSU 995 FA). The cover is removed and the TNF is cleaned before its installation into the vacuum chamber.

4.2.4 Cleaning procedure

Though the cover has been in place to protect the nanofiber, dust can settle on the TNF before the cover is being put on or after it has been removed. The nanofiber is first blown with a heat gun which remove bigger dust particles, if there are any. Then, it is dunked into

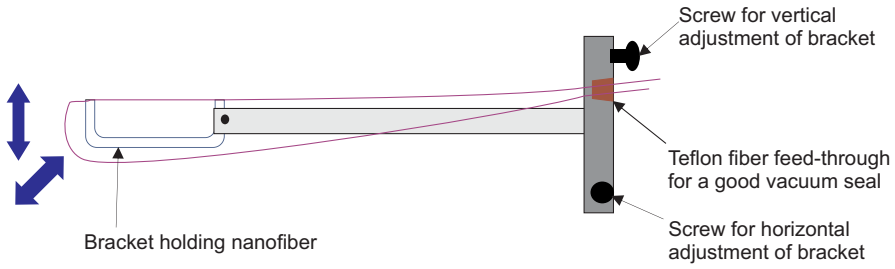

(a)

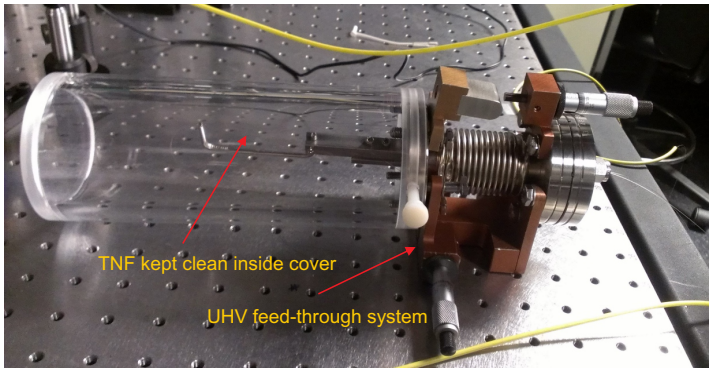

(b)

Figure 4.6: (a)Schematic and (b) picture of the UHV feed-through system

isopropyl alcohol (IPA) on a glass slide. These two cleaning processes sometimes improve the transmission of the nanofiber. Even if there is no improvement, at least the cleanliness of TNF is ensured which is crucial before inserting it into UHV.

The pre-pull cleanliness of the fiber is ensured by cleaning it with IPA as already mentioned in the steps of fiber-pulling in Sec. 4.1.1. There are a number of prerequisites and requirements (discussed in Sec. 4.4) that have to be taken care of for successful fabrication of nanofiber and introducing it inside the vacuum chamber.

For more discussion on the mechanism of taper-pulling and characterization of a taper, the reader is referred to [46, 47].

4.3 Estimation of the nanofiber profile by fiber-diffraction measurement

Once a nanofiber is fabricated, it is crucial to know its thickness profile, to ensure the required sub-micron diameter is reached. One obvious method to measure sub-micron thickness is to directly use scanning electron microscope (SEM). However, such a facility is not readily available and the task involved in this process is elaborate.

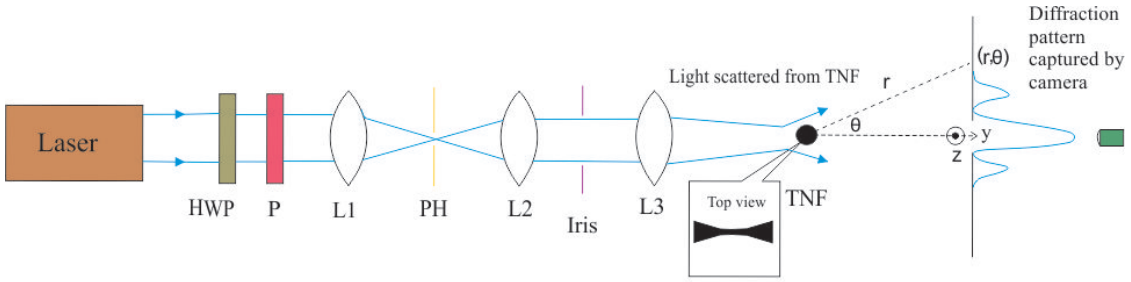

Figure 4.7: Schematic of fiber-diffraction measurement setup. A linearly polarized laser ($\lambda = 405$ nm) illuminates TNF at a point. The scattered light pattern is projected onto a screen and captured by a camera

Here, I will talk about a method (based on [25]) to measure the diameter of a tapered fiber by shinning a laser beam on the taper and from the diffraction pattern estimate the diameter. The experimental setup is shown in Fig. 4.7. A blue laser ($\lambda = 405$ nm) from a

laser pointer pen is first incident on a polarizer (P) and a half-wave plate (HWP) to orient the electric field polarization vector parallel or perpendicular to fiber axis. It is then subjected to spatial mode cleaning (lens L1 and lens L2 form a telescope and a pinhole PH filters the mode) and focussed on the tapered fiber by a lens (L3). The diffraction pattern pattern is projected onto the screen and captured by a camera. The situation is same as a theoretical problem of a plane wave of radiation being scattered on a infinitely long circular cylinder of homogeneous material (silica). The detailed calculations can be found in [35, 36] and I will just quote the results here. It is reasonable to approximate the Gaussian mode of a laser beam as plane wave because the nanofiber diameter ($\lesssim 0.5$ micron) is much smaller than the focussed beam width ($\approx$ hundred of microns). The diffraction geometry and coordinate system is shown in Fig. 4.7. The refractive indices of the medium and the fiber are given by n_1 and n_2 respectively. The angular field distribution in the far field is given by

$$I(r,\theta) = I_0 \Big| \sum_{m=-\infty}^{\infty} \exp\left[-im(\theta - \pi/2)\right] \times \left[J_m(n_1 k_0 r) - H_m^{(1)}(n_1 k_0 r)\gamma_m\right]\Big|^2 \tag{4.1}$$

where

$$\gamma_m = \frac{n_2 J_m(n_1 k_0 a) J_m'(n_2 k_0 a) - n_1 J_m(n_2 k_0 a) J_m'(n_1 k_0 a)}{n_2 H_m^{(1)}(n_1 k_0 a) J_m'(n_2 k_0 a) - n_1 H_m^{(1)\prime}(n_1 k_0 a) J_m(n_2 k_0 a)}, \quad (\mathbf{E} \text{ parallel to fiber}) \tag{4.2}$$

$$\gamma_m = \frac{n_1 J_m(n_1 k_0 a) J_m'(n_2 k_0 a) - n_2 J_m(n_2 k_0 a) J_m'(n_1 k_0 a)}{n_1 H_m^{(1)}(n_1 k_0 a) J_m'(n_2 k_0 a) - n_2 H_m^{(1)\prime}(n_1 k_0 a) J_m(n_2 k_0 a)}, \quad (\mathbf{E} \text{ perpendicular to fiber}) \tag{4.3}$$

Here, $k_0 = 2\pi/\lambda_0$ is the wave number; J_m and $H_m^{(1)}$ are the Bessel and Hankel functions of order m. A prime denotes the derivative of the function with respect to its argument. To note, the orientation of laser polarization relative to fiber affects only the coefficient γ_m.

(a) $E_{||}$ to fiber

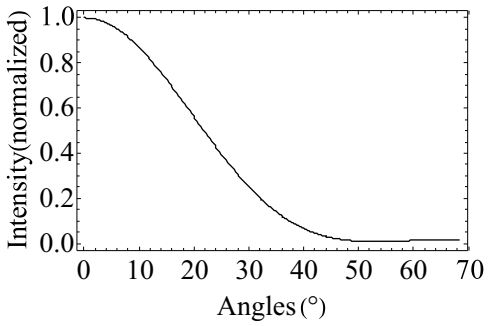

(b) $E_{\perp}$ to fiber

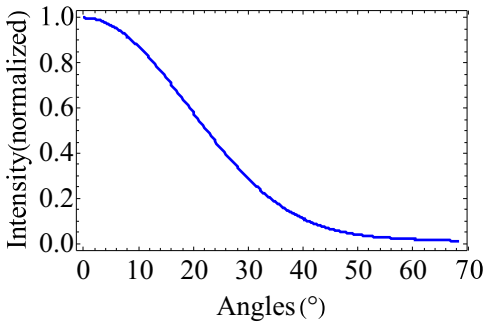

Figure 4.8: Theoretical normalized scattering intensity distribution for fiber radius= 210 nm at $\lambda = 405$ nm. For $E_{||}$ orientation, the first order minimum occurs at 52.94° but for $E_{\perp}$ orientation, there is no minima.

(a) $E_{||}$ to fiber

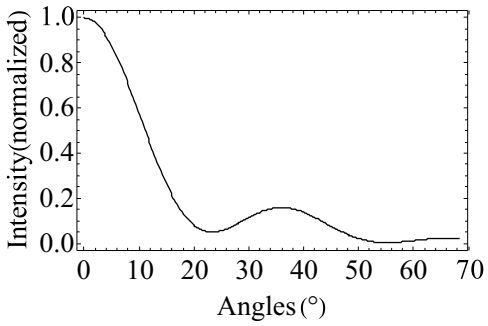

(b) $E_{\perp}$ to fiber

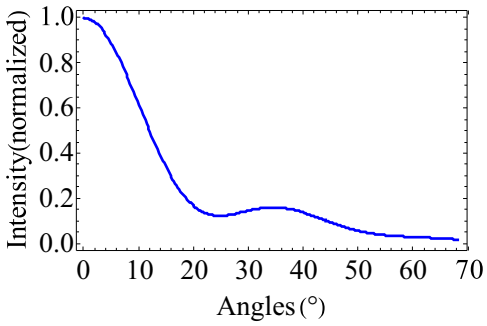

Figure 4.9: Theoretical normalized scattering intensity distribution for fiber radius= 375 nm at $\lambda = 405$ nm. For $E_{||}$ orientation, the first and second order minima occur at 23.38° and 55.23°. For $E_{\perp}$ orientation, the first order minimum occurs at 24.75°.

Some theoretical calculations and plots are done in Mathematica. The scattered field intensity distribution is found (by considering the 2^{nd} term in Eq. (4.1)) for different fiber radii. Fig. 4.8 and Fig. 4.9 show intensity distributions for both electric field orientations for radii 210 nm and 375 nm respectively. A set of angles for local minimum and maximum

(a) $E_{||}$ to fiber

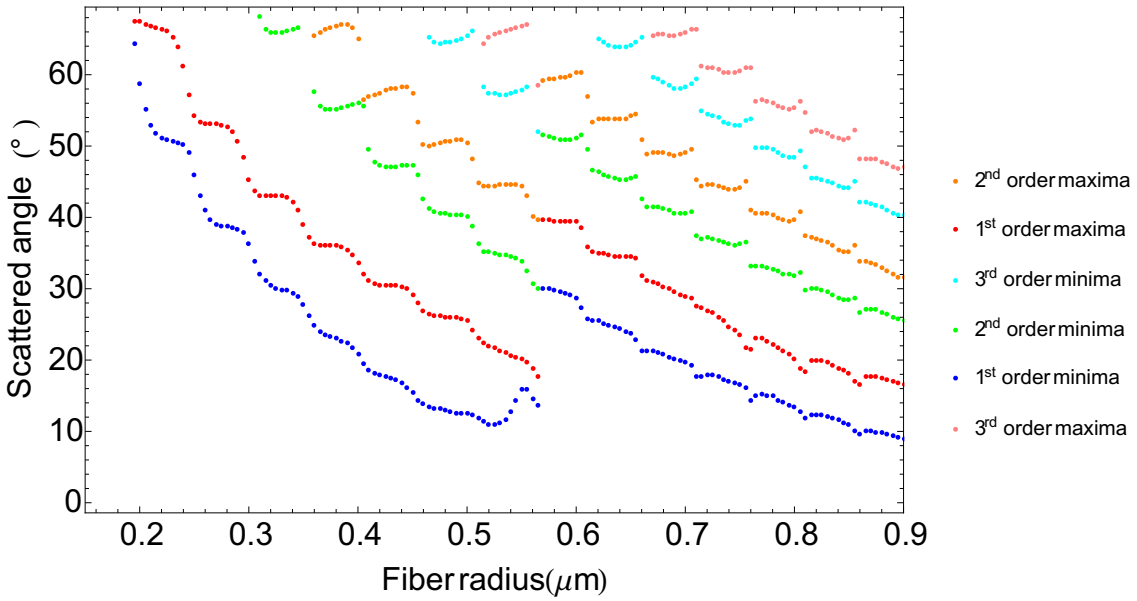

(b) $E_{\perp}$ to fiber

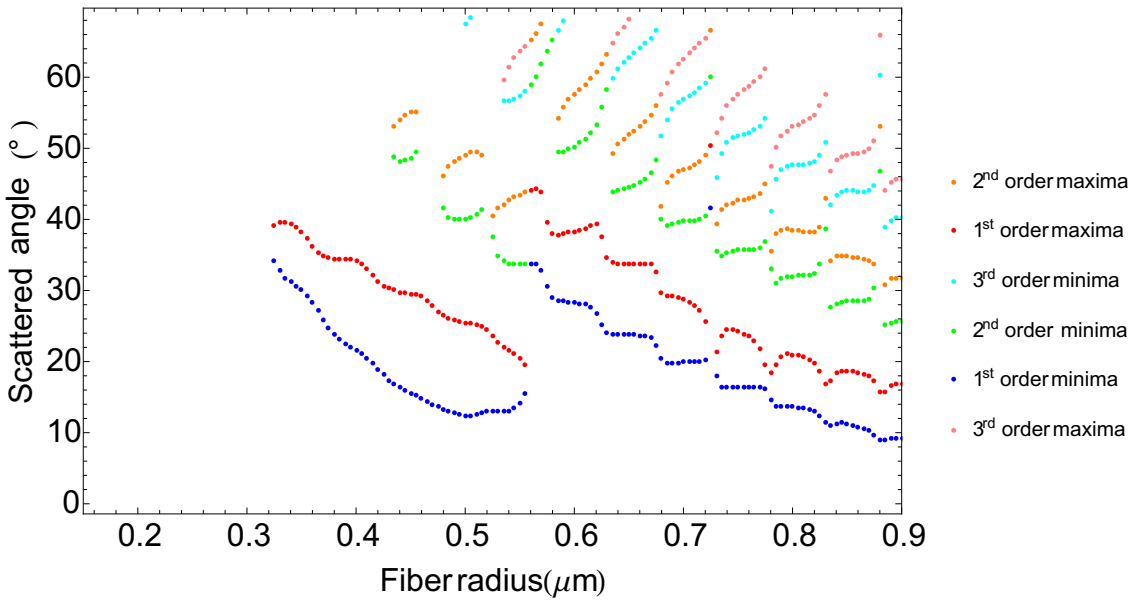

Figure 4.10: Radius-angle diagram showing the angles at which the scattered intensity has extremum values as a function of fiber radius

intensities for different fiber radii are computed and plotted against the fiber radius. Fig. 4.10 shows the radius-angle diagram for both field orientations. It is observed that for decreasing fiber diameter, the first order minimum vanishes first for perpendicular orientation and later for parallel orientation. Even for the parallel case, when the fiber diameter $\lesssim 500$ nm, the position of first order minimum for $E_{||}$ becomes less discernible (as seen in Fig. 4.8) until at around diameter ≈ 380 nm there is no first order minimum at all. This makes it difficult to estimate the nanofiber diameter by trying to directly locate the positions of extremum values from the scattered intensity distribution on screen. Moreover, due to errors the experimental intensity profile curve maybe displaced from its corresponding theoretical curve. Hence, it was necessary to analyze the image in Matlab.

The diffraction pattern on the graph paper, serving as a screen, is captured with a camera.

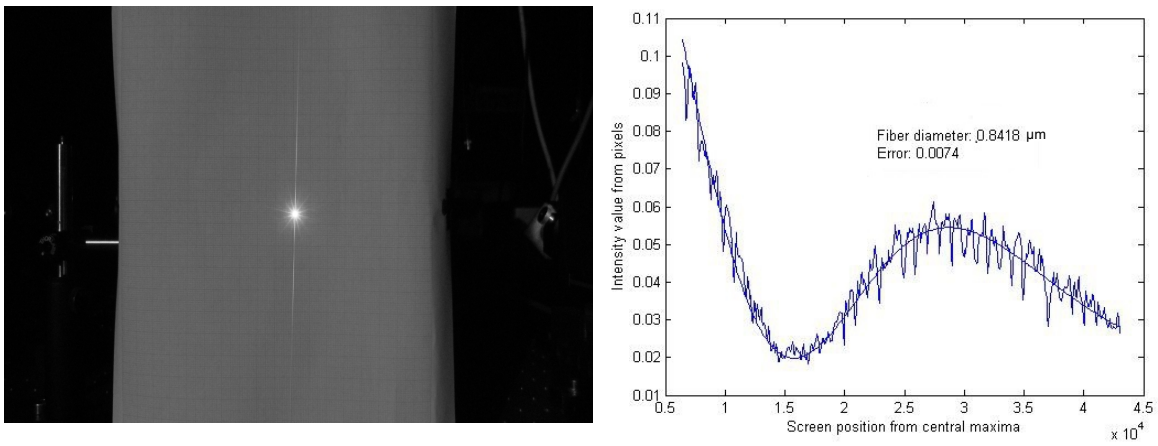

Figure 4.11: An example of the diffraction pattern captured by a camera and theoretical curve-fitting to that extracted intensity profile

The intensity profile is extracted from the image and the distance to pixel ratio is obtained by the help of the graph paper. Then, a Matlab code fits the experimental intensity profile with a theoretically calculated one by minimizing the error in curve-fitting. This technique helps to find the optimal value of fiber diameter for a given scattered intensity distribution. (Fig. 4.11). The process is repeated for different positions along the axis of the fiber taper

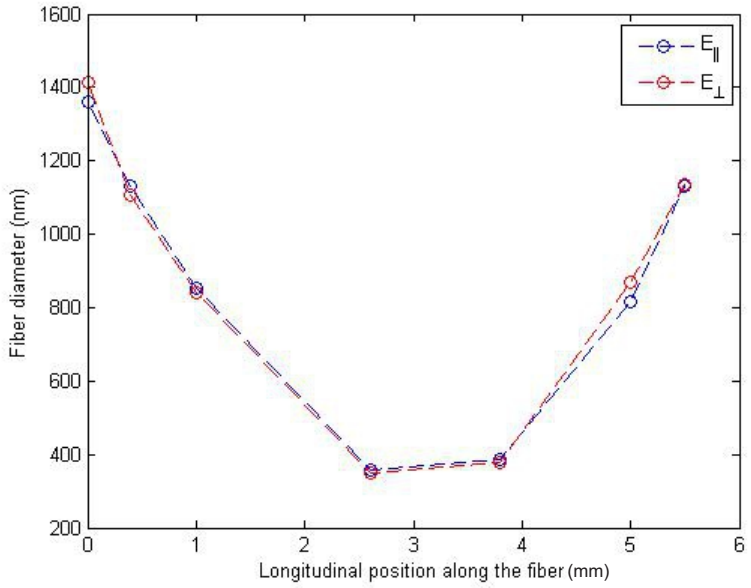

Figure 4.12: Profile of a tapered nanofiber for both parallel and perpendicular orientations of electric field relative to fiber axis obtained from fiber-diffraction measurement

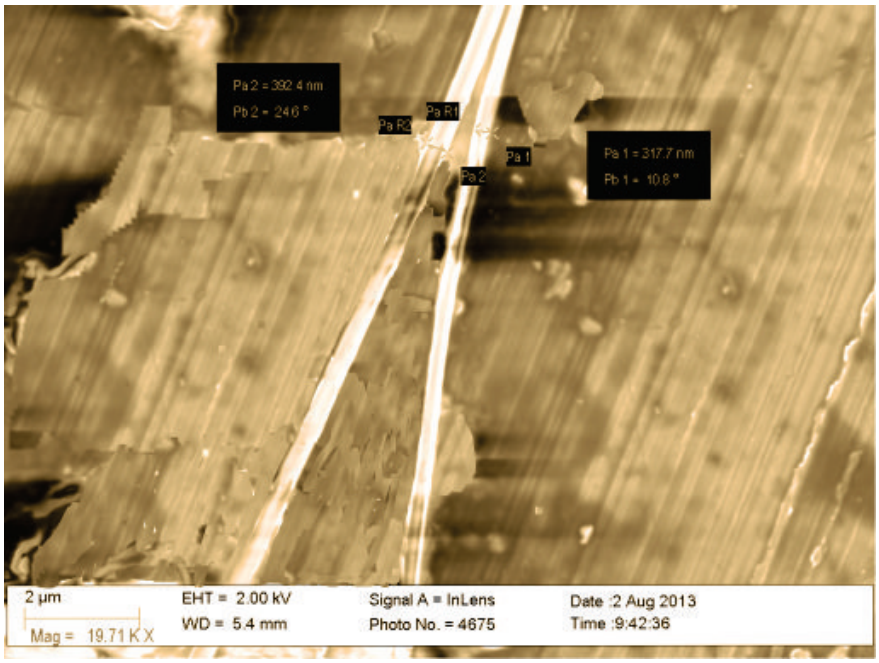

Figure 4.13: SEM picture of a broken TNF measured at two different points. The measured thicknesses are 392 nm and 318 nm

and subsequently the whole taper profile can be obtained. For our nanofibers, typically the taper waist is 1-2 mm and the diameter of the thinnest part is about $350 - 400$ nm (Fig. 4.12). This value from fiber diffraction measurement seems to agree reasonably well with the thicknesses (392 nm and 318 nm) measured by a SEM on the same nanofiber (Fig. 4.13).

4.4 Requirement and challenges

There are several challenges faced when fabricating nanofiber of the required diameter. I will mention them below :

- The nanofiber needs to have a small diameter of ≈ 400 nm for single-mode propagation at $\lambda = 780$ nm. Fabrication becomes increasingly hard with decreasing diameter as the sensitivity to imperfections increase. Moreover, the profile shape should ideally be an adiabatic one, where during the transition from the unstretched region to the tapering region and then the waist, the optical excitation stays at the fundamental mode. If higher order modes are excited it will lead to loss in transmission of the taper. Thus, manufacturing nanofibers with high transmission requires close to an adiabatic taper profile.

- If there are too many dust particles on the nanofiber then the nanofiber can melt in UHV when a laser field is sent through it. As dust particles scatter the evanescent light field at the tapered region, the nanofiber could get heated up beyond its melting point. This is because of limited thermal conduction of heat in UHV [49]. Hence the fiber cleaning procedure before and after the pull is important for survival of the TNF in UHV.

- When interfacing the nanofiber with MOT, atoms can fall onto the nanofiber surface and damage it. A blue laser $\lambda = 405$ nm with optical power between

10 μW and 100 μW is coupled into the nanofiber which possibly desorbs atoms from the nanofiber surface [20]. From experience, the longevity of the nanofiber has increased in the presence of blue light.

I have listed the parameters (or characteristics) of our fabricated nanofibers in Table 4.2 below.

TNF characteristic	**Value**
Diameter or thickness $2a_{TNF}$	300-400 nm
Transmission	$90-95\%$
Taper waist L_w	$1-2$ mm

Table 4.2: Characteristics of our TNF

Chapter 5

Experimental setup and methods

In this chapter, I will describe our experimental setup and the experiments performed on it. There are two main components to our experiment - MOT and TNF. In the first part, I will discuss the MOT setup and several of its components. I will go on to describe the steps that are followed for obtaining the MOT cloud and subsequently the experiments to estimate the relevant MOT parameters. Then, I will bring the tapered nanofiber (TNF) into the picture and discuss our efforts, by talking about a couple of experiments, to interface the MOT and the nanofiber.

5.1 Components of the MOT setup

The MOT setup has been built from scratch. When we started out, we just had a new metallic chamber, vacuum pumps and some remaining bits and pieces of the previous MOT setup (the details of that setup, which used a smaller glass vacuum chamber can be found in [14]). An experimental design was first sketched out with the help of Dr. Arturo Lezama, a visiting Professor in our group at the time. The components were bought and subsequently assembled over a period of time. Some of the components had to be designed and constructed by the scientific workshop at U of C.

5.1.1 Atomic transitions

We are using D2 lines of Rubidium 87 for our experiment. The cooling laser is detuned by 9 MHz below the closed-cycle transition $5S_{1/2}\ F = 2 \rightarrow 5P_{3/2}\ F' = 3$, which corresponds to an optical wavelength of 780.246 nm. Each cooling beam has an intensity of 6.1 mW/cm^2 (can be increased up to 8.1 mW/cm^2) The repumping laser is resonant with the transition

$5S_{1/2}\ F = 1 \rightarrow 5P_{3/2}\ F' = 2$, which corresponds to an optical wavelength of 780.232 nm. Each repumping beam has an intensity of 0.33 mW/cm^2. These transitions are shown in Fig. 5.1.

Detailed information on D2 transition of ^{87}Rb including Clebsch-Gordan coefficients can be found in Ref. [45]. I quote some important values in Table. 5.1

Parameters	**Symbol**	**Values**
D_2 Decay Rate/ Natural linewidth	Γ	$2\pi \times 6.065(9)$ MHz
D_2 Lifetime	τ	26.24(4) ns
D_2 Doppler Temperature	T_D	146μK
Dipole moment ($\sigma^{\pm}$- polarized light)	$d_{(m_F=\pm 2 \rightarrow m_{F'}=\pm 3)}$	$2.534(3) \times 10^{-29}$ C·m
Resonant Cross Section ($\sigma^{\pm}$- polarized light)	$\sigma_{0(m_F=\pm 2 \rightarrow m_{F'}=\pm 3)}$	2.907×10^{-9} cm^2
Saturation Intensity ($\sigma^{\pm}$- polarized light)	$I_{sat(m_F=\pm 2 \rightarrow m_{F'}=\pm 3)}$	1.669(2) mW/cm^2

Table 5.1: Properties of Rubidium 87

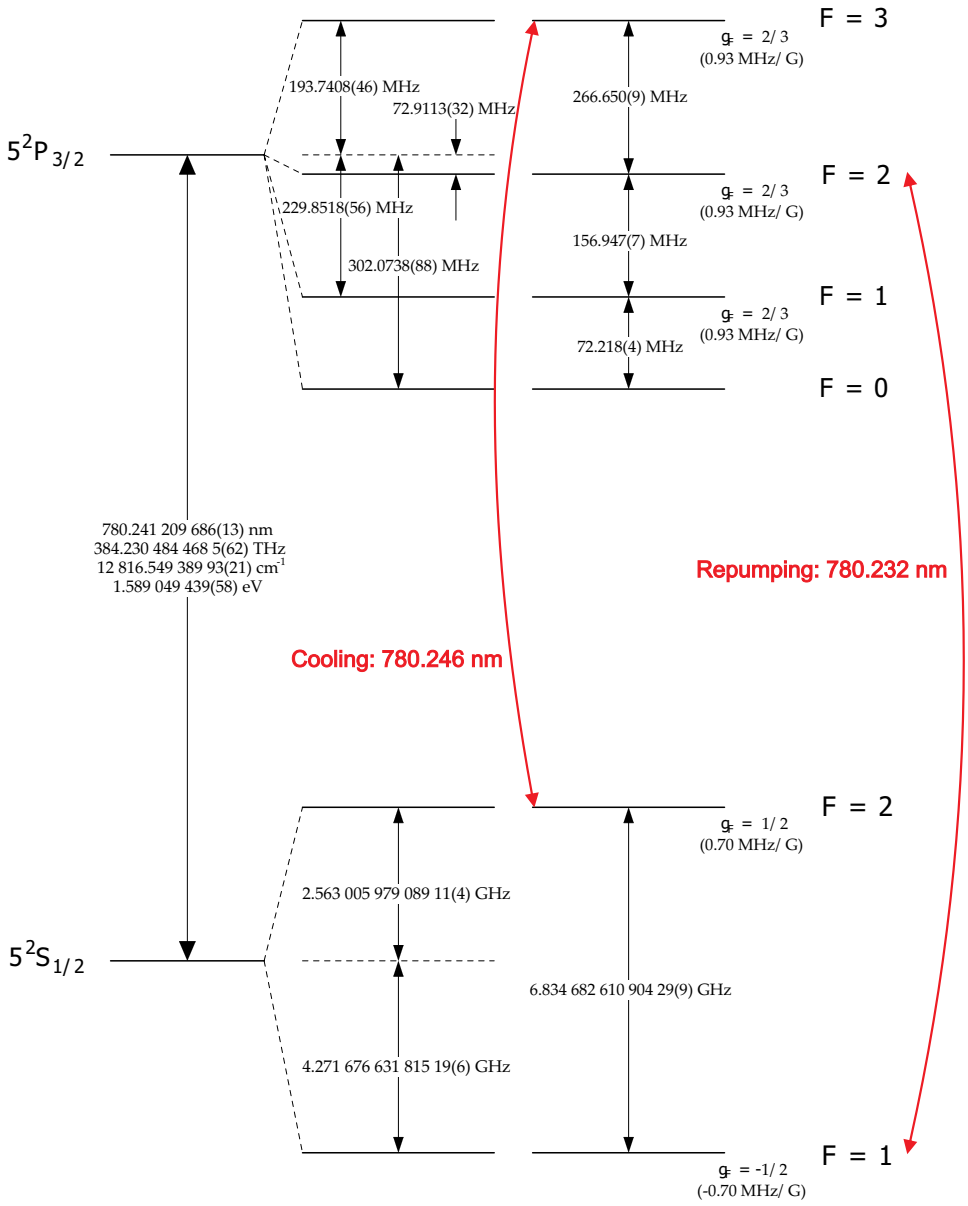

Figure 5.1: ^{87}Rb D_2 transition hyperfine structure from Steck [45] with the cooling and repumping transitions.

5.1.2 Vacuum system and Rubidium source

The vacuum chamber is octagonal in shape and made of stainless steel. Attached are 5 small glass view ports, commonly called 'windows' on each octagonal side and a couple of large view ports on either side. The internal diameter and thickness are 16 cm and 8 cm respectively. The chamber is placed vertically such that the large view ports lie in the vertical plane (as shown in Fig. 5.2). There are two pumps attached to this chamber. First is the turbo pump (Varian Turbo-V 81-M), supported by a mechanical dry pump (Agilent SH-110). This is used for reaching high vacuum environment. For reaching ultra-high vacuum (UHV) an ion pump (from Kurt J. Lesker) is operated. A valve between the turbo pump and the chamber is generally used for cutting off the chamber from the turbo pump system. After this cutoff, the ion pump maintains UHV environment inside the chamber. Our vacuum is at the threshold of UHV regime. The pressure gauge reading is typically between 4×10^{-9} and 3×10^{-8} Torr.

Source of rubidium atoms are Rb getters (Alkali Metal Dispenser 5G0125 Rb/NF/3.4/12 FT 10+10) from SAES group. They are attached to the chamber via a tube and conflat flange. The getters are welded to vacuum feedthroughs, which are then wired to a DC current supply. The current sent to the getters is usually $2 - 4$ A. This heats the rubidium salt coated on the getters and neutral Rb gas is released.

Bakeout and Degassing:

In this process, the vacuum system parts are heated to high temperatures, with the vacuum pumps switched on, to desorb water vapor and hydrocarbons from the vacuum parts. This process is also called degassing and it helps in lowering the pressure by a factor of 10 or more. In our case, we wrap the chamber and other vacuum parts (including the ion pump) with a thermal heating tape. A dc voltage is applied and the temperature is slowly raised (to avoid thermal stress) till it reaches 130°(the glass windows cannot withstand a temperature more than this). This process is continued for few days till the heating is stopped

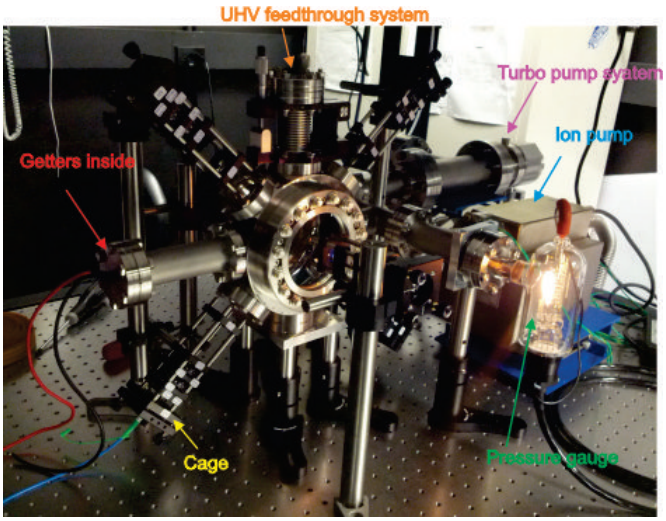

Figure 5.2: Picture of vacuum chamber and components attached to it

gradually. The pressure first increases when the baking has started, then it becomes steady and finally it decreases improving the over-all vacuum compared to pre-baking vacuum. We have performed the bake-out of our vacuum chamber a few times over a period of one and half years and each time the vacuum has improved a bit.

The pressure gauge (from Kurt J. Lesker) attached next to the ion pump has a 'degassing' facility, which has been found to improve the vacuum (as well as the performance of ion pump) especially after the rubidium getter has been used for a long time.

Every time after we break the vacuum, we have to change the copper gasket and ensure that the vacuum is sealed. Quite often, there is some leak and the pressure refuses to go down. In that case, we have detected the leak by using Helium leak detector (or if there is a sudden drop in pressure by sprinkling alcohol at joints, it also implies a possible leak) from the group of Prof. Nasser Moazzen-Ahmadi.

5.1.3 'Cage' optics

The repumping and the cooling beams are coupled via polarization maintaining fiber (PMF) patch cables, into two input ports of a two-to-six fiber beam splitter. Its six output ports are connected to the six 'cages' via PMF patch cables. The 'cage' (as shown in Fig.5.3) contains

optical components to transform a linearly polarized beam into a circularly polarized beam. In addition, it expands and collimates the MOT beams.

The light diverging out of a fiber is collimated by lens (L1), the polarizer (P) allows the linear polarization to pass through (the angle of polarizer can be varied to vary the output power), quarter-wave plate (QWP) transforms the linearly polarized light into circularly polarized light and finally the telescope (formed by lens L2 and L3) at the end produces a beam of diameter 2.5 cm. It is ensured that light coming out of the opposite cages are σ^+ and σ^- (with respect to the atomic quantization axis aligned with the light propagation direction).

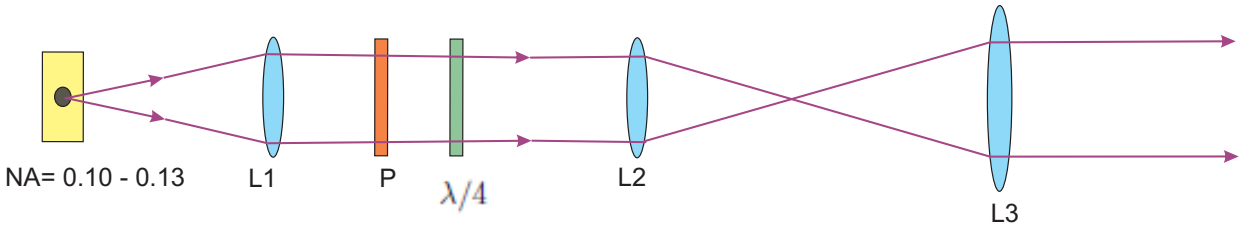

Figure 5.3: Optical components of a 'cage'

5.1.4 Magnetic coils

The magnetic coils are made of copper wires, 4 mm thick, and wound around a non-conducting ring. There are 400 turns for the main coils and the compensation coils have a smaller number of turns. The main coils have a diameter of 16 cm and they are apart by 8 cm. The two coils are connected in series with a current source which can supply current up to 10 A. The magnetic field gradient at center is 10 G/cm for a current of 2 A, which is

reasonable for a MOT.

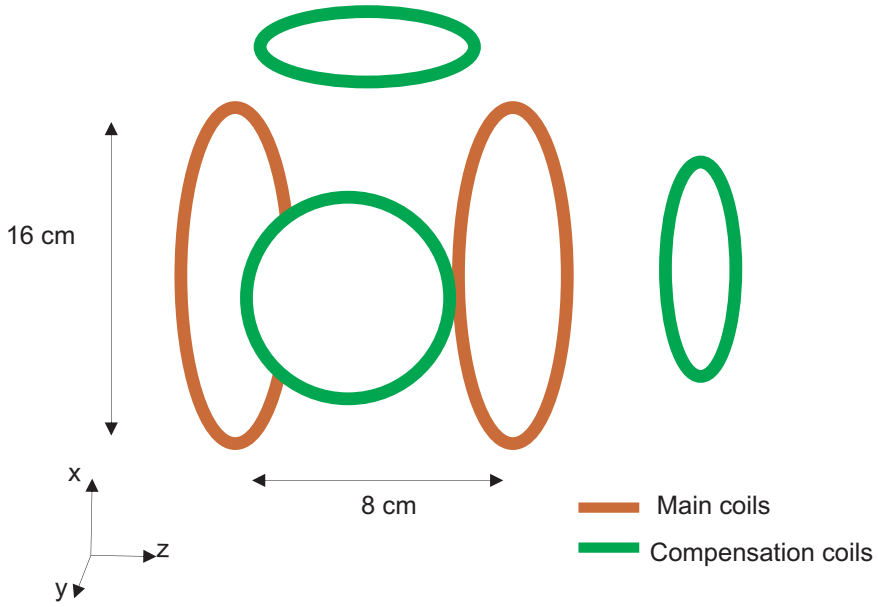

Figure 5.4: Magnetic coils around the vacuum chamber with the plane of chamber lying in x-y plane

It is required in our experiment to move the MOT cloud in order to overlap with the nanofiber (discussed in Sec.5.6.1). This is accomplished by using the compensation coils in all three dimensions (shown in Fig. 5.4). This additional magnetic field helps to move the center of the trap by shifting the center $B = 0$ in space.

5.2 Saturated absorption spectroscopy and frequency locking

Since the trapping forces in MOT are sensitive to detuning of the cooling laser from the atomic transition, the range of detuning in which a MOT cloud can be formed is limited to about -20 to -25 MHz. Unfortunately, the frequency of cooling laser drifts out of this range and so it has to be locked by an electronic frequency locking circuit to a reference frequency signal. A particular transition in the saturated absorption profile of ^{87}Rb is chosen as the reference signal. The principle of saturated absorption spectroscopy and the locking

technique will be described in this section.

There is no need to lock the frequency of the repumping laser. This is because it is less sensitive to small frequency drifts. For a relatively large drift, the repumping laser will possibly address some other transition to one of the hyperfine levels or Zeeman sublevels in the excited state effectively removing the atoms from $F = 1$. We scan the repumping laser to make sure it is in resonance and observe the Doppler-broadened absorption profile.

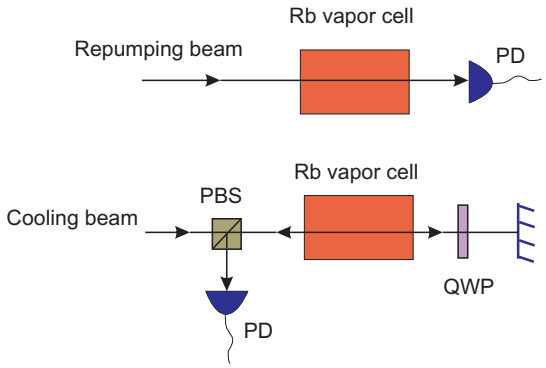

Figure 5.5: Schematic of Doppler spectroscopy for repumping laser (above) and saturated absorption spectroscopy for cooling laser (below); PBS- Polarizing beam-splitter, QWP- Quarter waveplate, PD- Photodetector

The atoms at room temperature (or in hot gas system) have a Maxwell's velocity distribution. Hence, each atom will interact with radiation in a different way because of the frequency detuning, caused by the Doppler effect. The absorption line shape is Gaussian and this kind of inhomogeneous broadening is commonly referred to as Doppler broadening. This is a predominant contribution to the observed width of lines in atomic spectra. Fig. 5.6 shows the Doppler-broadened profile as the repumping laser is made to single pass a rubidium cell. The width of the Doppler-broadened line is 502 MHz for ^{87}Rb.

A Doppler-free laser spectroscopy technique called saturated absorption spectroscopy is used to counter the effect of Doppler broadening. This is performed for the cooling laser in

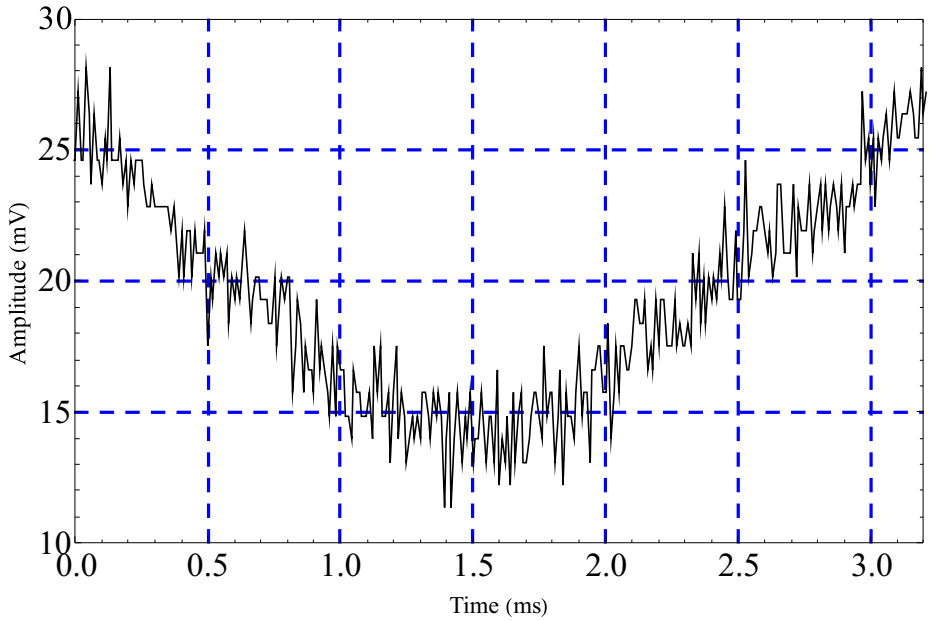

Figure 5.6: Doppler-broadened absorption line for ^{87}Rb D_2 transition

our experiment. In this technique a laser beam is made to double pass a vapor cell. Each beam will be resonant with a set of velocity groups. If a velocity group can be addressed by both, it will absorb the forward beam which has more intensity compared to the reflected beam. This will create a transparency window for the back reflected beam.

With this configuration, there are two types of velocity groups that can addressed by both beams. The first is $v = 0$, which will be addressed by the resonant frequencies of the transitions. $F = 2 \rightarrow F' = 3$ transition in Fig. 5.7 is an example of such a case. The second is the velocity group that comes into resonance (ω_1) with an atomic transition because of the blue-detuned Doppler shift to the forward beam while coming into resonance (ω_2) with some other transition because of the red-detuned Doppler-shift to the reflected beam. That is there is a velocity group that is simultaneously resonant with two different transitions, $\omega = \omega_1 + kv = \omega_2 - kv$ and the transparency is created at $\omega = \frac{\omega_1+\omega_2}{2}$ between the two resonances. $F = 2 \rightarrow F' = 1, 3$ and $F = 2 \rightarrow F' = 2, 3$ in Fig. 5.7 are the two crossover peaks.

The cooling laser is locked by the help of a lock-in amplifier on the crossover peak $F' =$

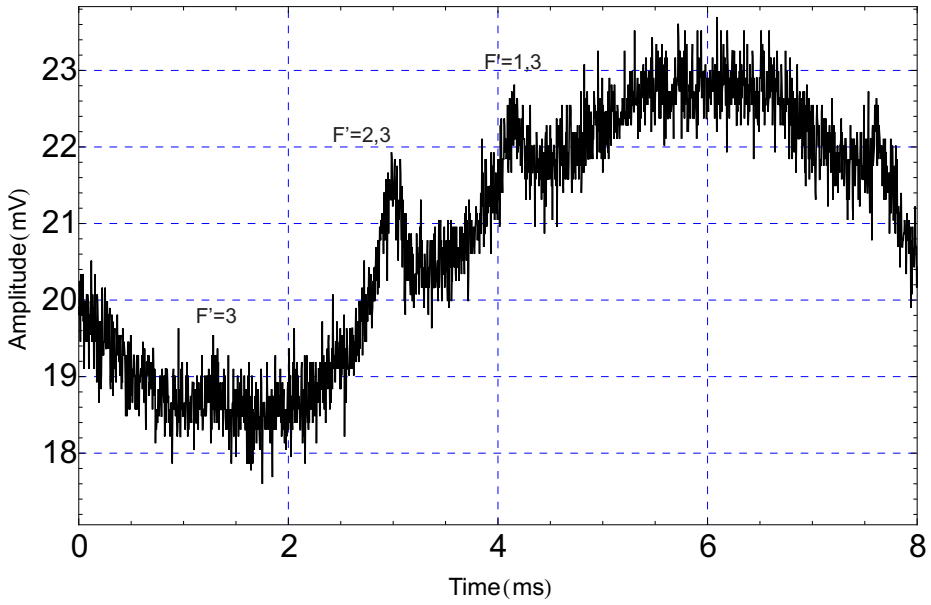

Figure 5.7: Saturated absorption signal for ^{87}Rb D_2 transition showing $F = 2 \rightarrow F'$ transition peaks

2, 3. This peak is chosen because after locking, the required amount of frequency shift needed for addressing the cooling transition can be provided by the acousto-optic modulator (AOM) (Appendix A.3). In other words, the required value of the frequency shift falls within the bandwidth of our AOM used. Also, this crossover peak has the strongest signal among the $F = 2 \rightarrow F'$ transitions. The schematic of locking is shown in Fig. 5.8. The atomic spectroscopy signal from photodetector (PD) is mixed with the dither (reference) signal from function generator and sent to the lock-in amplifier. Depending on how much the laser frequency is displaced from the center of the crossover peak, a feedback signal is generated to bring the laser frequency back to the center of the peak. The feedback dc voltage signal is applied to the piezo of the laser to shift the laser emission frequency close to the atomic reference frequency.

A brief discussion on the working principle of our home-made lock-in amplifier [26] is given in Appendix A.4.

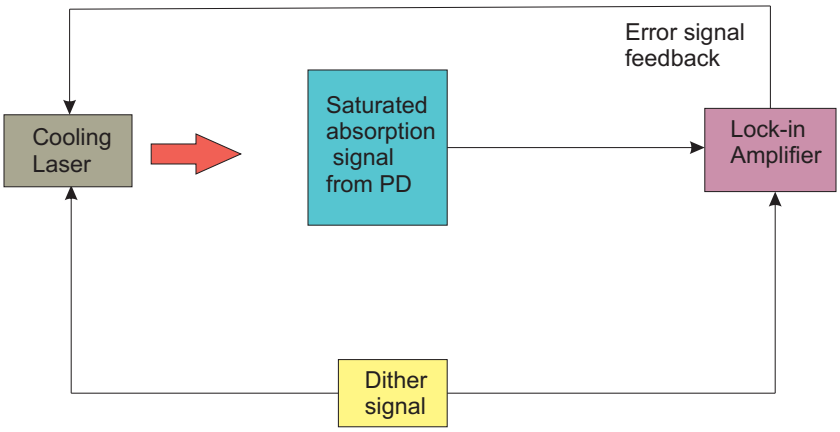

Figure 5.8: Frequency locking scheme used for the cooling laser

5.3 Experimental setup

The full experimental layout is shown in Fig. 5.9. In the bottom-half of this layout, there are the cooling and the repumping lasers, both of which are external cavity diode lasers (description of ECDl in Appendix A.1) with diodes from Axcel Photonics. This part of the layout is to prepare the lasers with correct frequencies for the MOT. The frequency of repumping laser is checked (by Doppler spectroscopy) and the frequency of the cooling laser is locked to 2,3 crossover peak in saturated absorption spectroscopy (by lock-in amplifier as discussed in previous section). For the repumping laser, there is an AOM (1205C-x Isomet) in the beam path after the spectroscopy part. The purpose of the AOM is to switch on-off the beam for the experiments. For the cooling laser, the frequency needs to be shifted to 9 MHz below the cooling transition and this is accomplished by the AOM in its beam path. This AOM also performs the switching on-off operation of the cooling beam for the experiments. Next, there is a tapered amplifier (TA) which amplifies the cooling laser by a factor of 30-40. This high power is for the six cooling beams required for the trap. Finally, both the cooling and the repumping lasers are coupled to polarization-maintaining (PM) optical fibers by

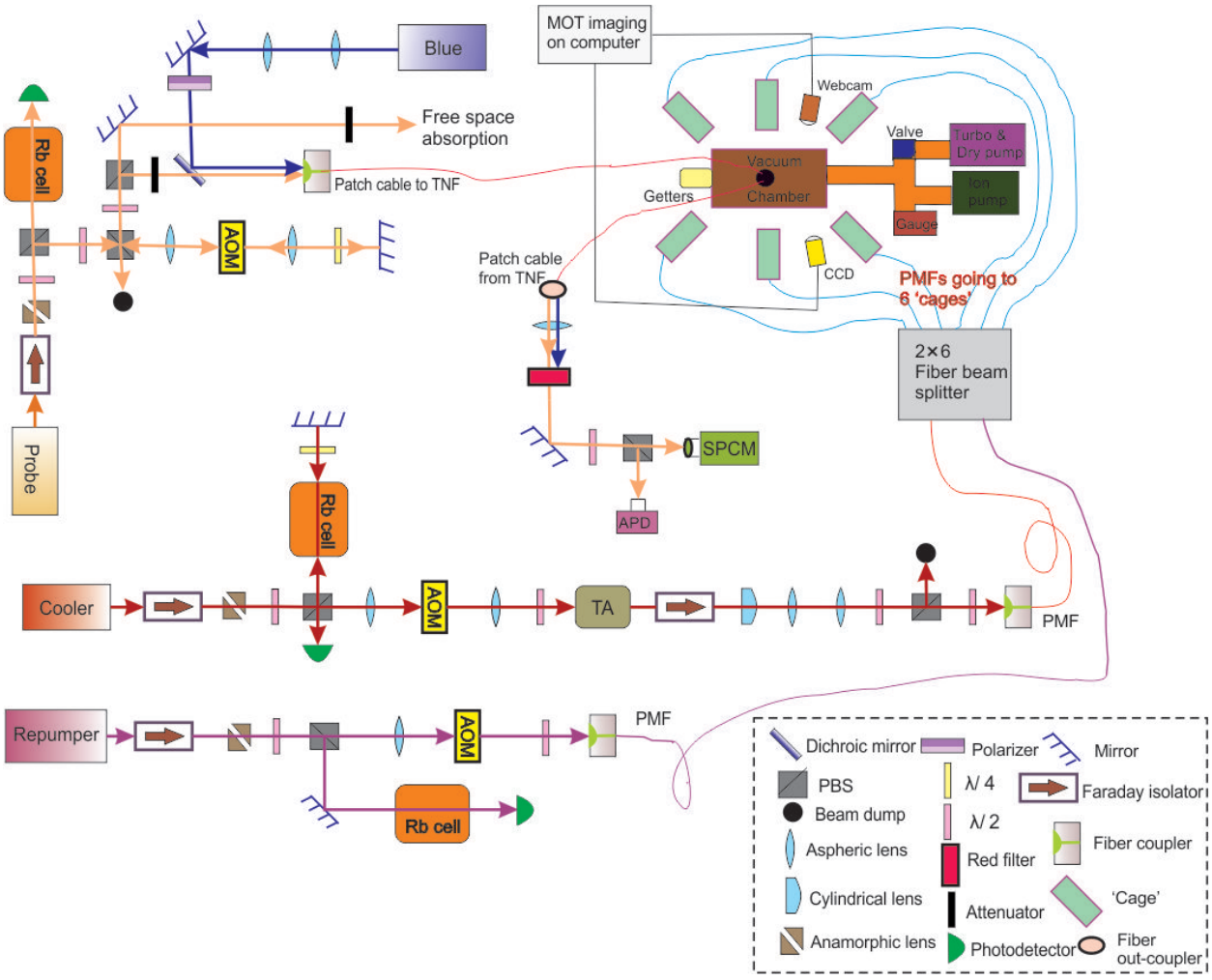

Figure 5.9: Complete experimental setup

means of fiber-coupling stages and sent to a 2×6 fiber beam splitter (Evanescent Optics). The fiber beam splitter combines the cooling laser with the repumping laser, and divides among its six output ports, which are then fiber-connected to six different 'cages', around the vacuum chamber.

Now we are in the top-half of the layout. The probe laser (ECDL with an Eagleyard diode) has to be prepared for probing the MOT cloud. The probing is done by either injecting a free-space beam as is done in one experiment or by sending it though the nanofiber as is done in the other one. The probe beam is divided into two parts. One goes to a rubidium cell for checking the laser frequency (Doppler spectroscopy) and the other is made to double pass an AOM. The AOM is used for switching on-off the probe beam as well as provide a laser scan (discussed in Sec. 5.4). After passing through the AOM, the probe beam is again split into two parts by combination of half-waveplate ($\lambda/2$) and polarizing-beam splitter (PBS). One part of the beam is used for free-space absorption experiment (Sec.5.5) while the other part is coupled into the nanofiber for evanescent field spectroscopy on cold rubidium atoms (Sec.5.6.3).

The probe light coupling out of TNF is first collimated by a lens and then passed through a set of red filters (for eliminating the blue laser). It is then either detected by single photon counting module (SPCM) (Perkin Elmer SPCM-AQR series) or avalanche photodiode (APD; silicon diode C30902E) depending on the requirement of the experiment.

Procedure for obtaining the MOT cloud:

The process of transfer, manipulation and introduction of TNF into UHV has already been discussed in Sec. 4.2 of Chapter 4. Once the TNF is safely installed inside the chamber and the vacuum is sealed, we go on to the next part of the experiment, whose steps are as follows:

- The powers of the cooling and repumping beams are monitored. Generally, the optical alignment to AOM, TA need to be checked and coupling to the PM fiber have to be adjusted to get optimal output power of typically between

16 and 40 mW for the cooling laser. Below this range the MOT cloud looks 'dimmer' which means the atomic density is less and above this range the power can saturate the atoms in the MOT. So based on experience, the power is kept at 30 mW (Intensity= 6.1 mW/cm^2) for each cooling beam. The same procedure is repeated for the repumping beam, except that there is no TA in this case, till we get 1.6 mW (Intensity= 0.33 mW/cm^2) for each repumping beam.

- Both the cooling and the repumping lasers are kept on laser scan. The current to the getters (between 2-4 A) is turned on. From the CCD camera (positioned close to the vacuum chamber as seen in Fig. 5.9), the fluorescence from the Rb atoms is observed.

- Both the laser scans are stopped. The current to the main coils is turned on and one can see a 'ball' of fluorescence about the center of the vacuum chamber. This is the MOT cloud (Fig. 5.10). The detuning for each of these lasers is adjusted slightly to make this 'ball' as bright as possible.

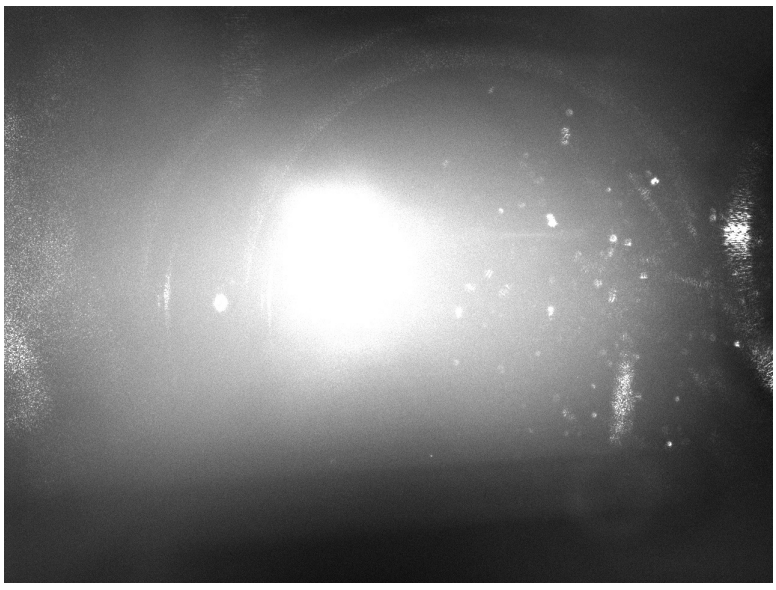

Figure 5.10: ^{87}Rb MOT cloud

5.4 Switches for the experiment

In an experiment to probe the atomic cloud with the probe beam, the MOT beams and magnetic field if kept on, will influence the atoms and in turn influence the results of that experiment. So to overcome this limitation, we have developed switching techniques for switching on and off the cooling beam, the repumping beam, the probe beam and the magnetic field. The important role played by the switches in the experiment will become apparent as we go on to Sec. 5.5 & 5.6.

It is necessary for all the switches to be synchronized to each other. For that purpose, a pulse delay generator (BNC 565) is used. It serves as a 'central clock' which outputs synchronized TTL signals (i.e. 0-0.5 V $\rightarrow$ logic 0; 4.5-5 V $\rightarrow$ logic 1) of adjustable pulse width and delay. The TTL signal acts as a trigger for each of the switches.

Magnetic coil on-off switch

The circuit used for switching current in the main coil is shown in Fig. 5.11. The first part

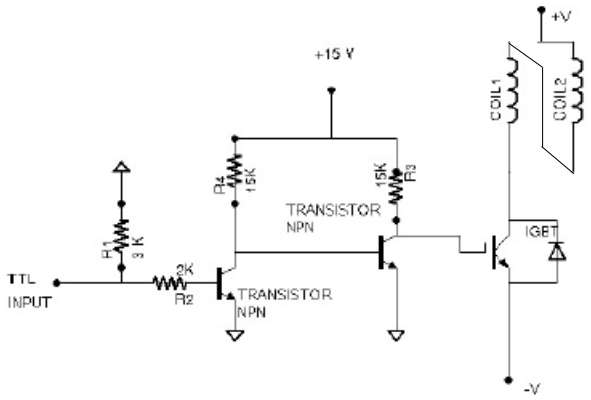

Figure 5.11: Schematic of magnetic coil on-off switch taken from Lucia Duca's thesis [23]

of the circuit, with two npn transistors, basically works as an inverter. The second part of the circuit has an industrial grade insulated bipolar transistor (IGBT) which operates in saturation region or cutoff region based on the TTL input. The advantage of IGBT is that it

has high current rating combined with high efficiency fast switching performance. Thus, the magnetic coil current typically between 1.5 A and 8 A can be switched on and off without heating of the switch.

MOT beam on-off switch

This switch is used for the MOT beams (cooling as well as repumping beams). The TTL input is given as the external modulation to the function (or waveform) generator. The output of the function generator is a modulated sine wave which is amplified by the radio-frequency (RF) amplifier and fed to AOM. The AOM has been set up for a single pass such that only the first order diffracted beam is allowed to pass through. The existence and non-existence of the first order beam is governed by the modulated sine wave input.

Probe beam on-off switch with laser scan

This is similar to the MOT beam on-off switch, except now that the laser has to be scanned

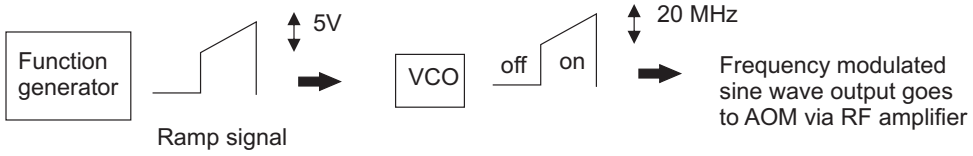

Figure 5.12: Scheme of probe beam on-off switch. When it is 'on' the laser is scanned over 40 MHz.

when the switch is 'on'. The switch is used for the probe beam, which we want to scan for 30-40 MHz (covering the absorption linewidth of cold atoms $\approx$ 6 MHz) about the resonance for the purpose of spectroscopy. This is achieved by using a voltage controlled oscillator (VCO) (Appendix A.5). A ramp signal of 5-10 V, as shown in Fig. 5.12, is applied from an arbitrary waveform generator to the VCO which provides a frequency modulation in the

range from 63 MHz to 83 MHz i.e. $\delta f = 20$ MHz. The frequency range is chosen to match the AOM bandwidth (60 MHz - 90 MHz). This frequency modulated oscillation signal from VCO goes to AOM via RF amplifier. The AOM is set up for the double pass configuration. In this configuration, the probe beam is made to pass through the AOM twice, so that effectively the probe beam is scanned for $2(\delta f) = 40$ MHz i.e., from 126 MHz to 166 MHz, when the switch is on. The switching on-off mechanism is the same with that of the MOT beam on-off switch.

5.5 Absorption of a free-space probe beam by the MOT cloud

A part of the probe beam is injected into the MOT cloud for spectroscopy on cold rubidium atoms. This experiment will help to estimate some crucial MOT parameters, like the number of atoms in the trap, the size of the cloud and the cloud density. Also in this experiment, we can test our switches for the MOT beams, the probe beam and the magnetic field. The free-space spectroscopy with switching, will help us to find the characteristic time-of-flight of the atoms released from the MOT i.e., the time for which the trap is not depleted of atoms after the MOT beams and the magnetic field are switched off. This parameter is important for the evanescent field spectroscopy on cold rubidium atoms (discussed in Sec. 5.6.3).

When the probe beam is injected into the cloud with few milliwatts of power, one can see the cloud mechanically displaced (looks as if the MOT is 'eaten up') with the CCD camera. This process helps to determine experimentally if we are able to 'hit' the MOT at the center. The diameter of the probe beam is adjusted by changing the position of the lens so as to ensure that the MOT is optimally 'hit' by the probe beam. Under this optimal condition, the probe beam is just able to cover the entire atomic cloud and the cloud completely disappears when 'hit' by the probe. At this point, the MOT diameter is roughly equal to the diameter of the probe beam. Therefore, from this technique the diameter of the MOT has been estimated to be $d_{MOT} \approx 3.5$ mm.

In experiment, the probe beam of power 8 μW is injected into the cloud. After the passage of the probe through the cloud it is focussed onto a photodetector. The intensity of probe beam is around 0.083 mW/0036cm^2, which is much less than the saturation intensity 1.67 mW/cm^2 and so has negligible mechanical effect on the atomic cloud.

Without switching:

With the MOT beams, the probe beam and the magnetic field kept on, we observe $65-70\%$ absorption (shown in Fig. 5.13) of the probe beam by the MOT cloud when the laser is scanned over a GHz. This implies an optical depth (OD) of 1.2 where the optical depth of a medium is given by $OD = -\ln\left(\frac{P_{out}}{P_{in}}\right)$ where P_{out} is the transmitted power, P_{in} is the input power to the medium.

The absorption linewidth for ^{87}Rb is ≈ 6 MHz. The linewidth for cold atoms is relatively narrow with respect to the broadened linewidth of atomic vapor. This is one reason why cold atoms are used extensively for experiments in atomic physics. Though the probe beam is weak enough not to disturb the trapping mechanism, one must take into account that the probe beam will be competing with the MOT beams as far as absorption of light by the atom is concerned. This is because the atoms only in the ground state will absorb the probe beam and hence will not participate in the cooling process. The ground state population ρ_{gg} for a two-level system (simplified picture) is given by

$$\begin{aligned} \rho_{gg} &= 1-\rho_{ee} \\ &= 1-\frac{1}{2}\frac{\Omega^2}{(\Gamma/2)^2+\Delta^2+\Omega^2/2} \end{aligned} \tag{5.1}$$

where Ω is the Rabi frequency, Δ is the frequency detuning to resonance, Γ is the decay rate. With the values of $\Omega = 14$ MHz, $\Delta = 9$ MHz, $\Gamma = 2\pi \times 6$ MHz in our case, $\rho_{gg} = 55\%$ i.e., 55% of the atoms in our MOT are in the ground-state.

From the strength of absorption signal, the number of atoms in the MOT and subsequently the density of the cloud are estimated. According to the Beer-Lambert law,

$$\frac{I_{out}}{I_{in}} = \exp(-\sigma n l) = \exp(-\sigma\frac{N}{A}) \tag{5.2}$$

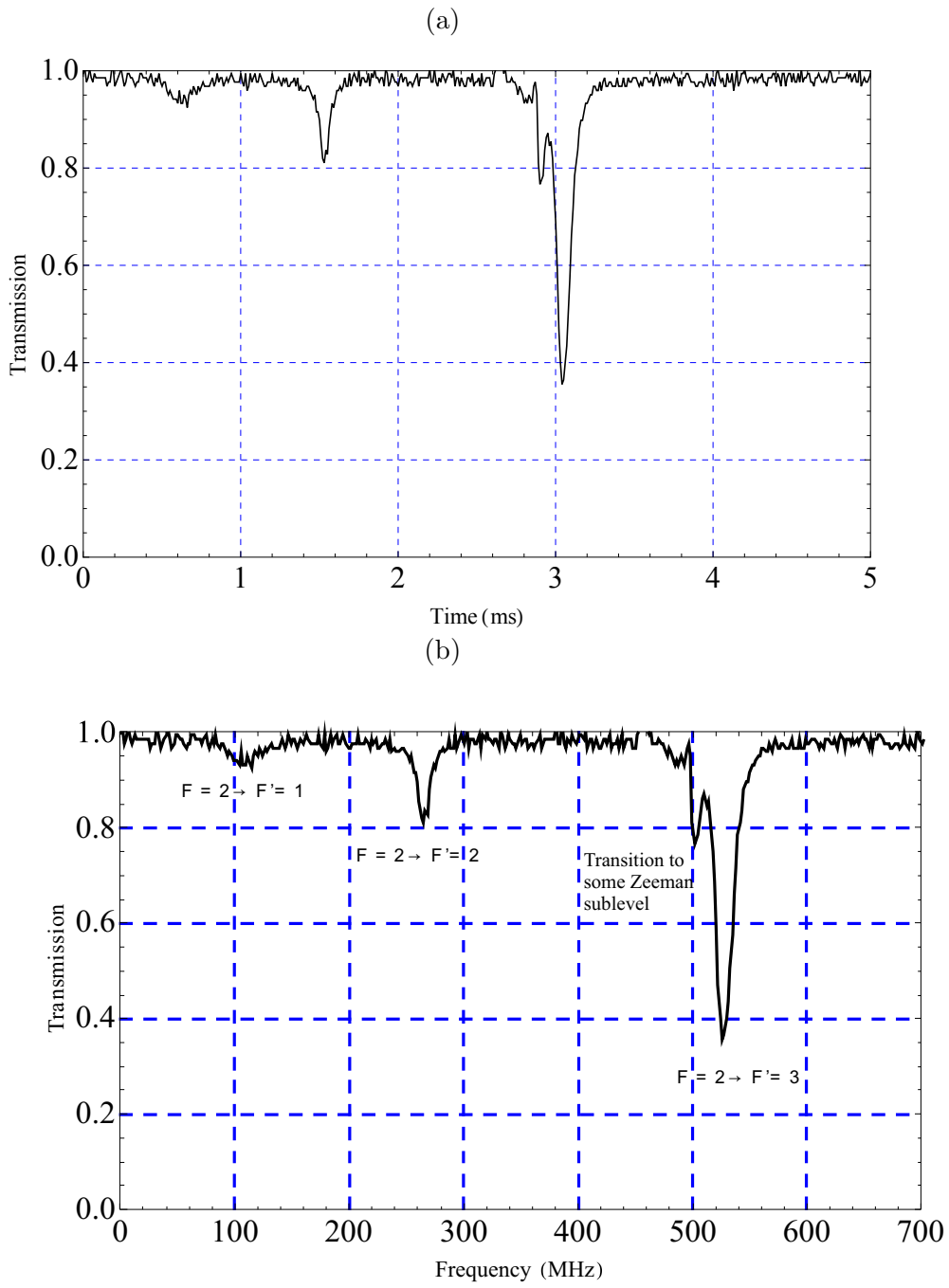

Figure 5.13: Absorption profile of ^{87}Rb MOT cloud with the probe laser (8 μW) scanned over a GHz about the D_2 transition. The x-axis is in (a) time, as recorded by the oscilloscope and (b) frequency, converted from time using a Doppler-broadened reference signal. The dips correspond to the following transitions: $F = 2 \rightarrow F' = 1$, $F = 2 \rightarrow F' = 2$, some Zeeman sublevel transition and $F = 2 \rightarrow F' = 3$ with frequency increasing (from left to right).

where I_{out} is the transmitted intensity, I_{in} is the input intensity, σ is the scattering cross section (value in Table 5.1), n is the atomic density, l is the length of medium travelled by light, N is the total number of interacting atoms and A is the probe laser beam area. If N_0 be the total number of atoms in the ensemble, then the number of atoms taking part in the absorption is $N = N_0\rho_{gg}$. Hence, the total number of atoms in the MOT is

$$\begin{aligned} N_0 &= \frac{N}{\rho_{gg}} \\ &= -\frac{A}{\sigma\rho_{gg}} \ln\left(\frac{P_{out}}{P_{in}}\right) \end{aligned} \tag{5.3}$$

The total number of atoms from absorption detection is found to be $N_0 = 6.33 \times 10^7$ by substituting the known values. With the known cloud size i.e., $d_{MOT} \approx 3.5$ mm, the atomic density of the cloud is estimated to be $\rho_{MOT} = 2.82 \times 10^9$ per cm^{-3}. These values are well within the expected range for a standard MOT [44].

With switching:

The timing sequence of the switches are shown in Fig. 5.14. During the first 6 ms, the atoms are cooled and captured in the MOT while the probe laser is off. In the following 2 ms, the cooling and the repumping lasers as well as the magnetic field are switched off while the probe laser is turned on. During this period the probe laser is scanned by the AOM. The design and implementation of all the switches have already been described in Sec. 5.4. In principle, one expects to see more absorption in this case compared to the previous case where no switching is done. This is because now the free-spectroscopy on the atomic cloud is not influenced by the MOT beams and the magnetic field anymore. However, $45 - 50\%$ absorption (shown in Fig. 5.15) has been detected with switching in our case.

The upper limit of the probe laser pulse duration is governed by the characteristic time-of-flight of the atoms released from the MOT. It has been observed that the MOT beams and magnetic field cannot be switched off for more than $2 - 3$ ms for optimal absorption signal in this experiment. If this duration is prolonged beyond 3 ms, the absorption signal becomes weaker as the trap starts getting depleted of atoms. The time-of-flight of the

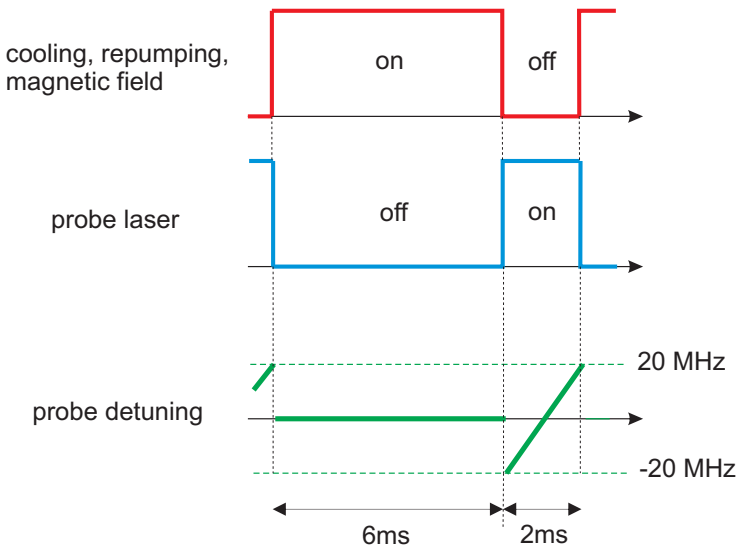

Figure 5.14: Timing sequence of the experiment

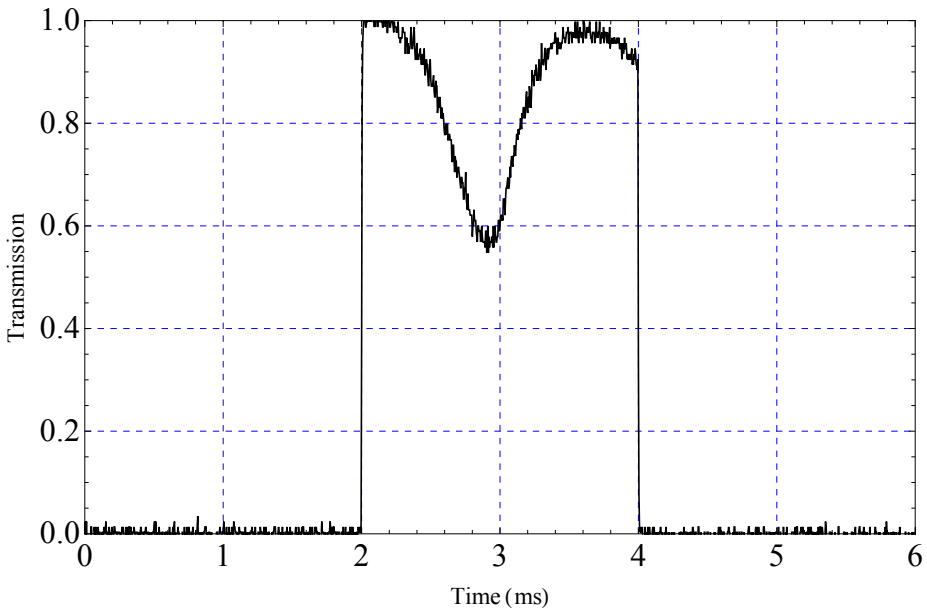

Figure 5.15: Absorption profile of ^{87}Rb MOT cloud when the above switching sequence Fig. 5.14 is operated. The probe beam is scanned over 40 MHz.

atoms is primarily influenced by the MOT temperature (atoms move away because of their velocities) and the force of gravity (atoms fall down). It is also affected by the background pressure (typically 9.8×10^{-9} Torr for our vacuum chamber). Based on the time-of-flight measurement, this same timing sequence has been used for the evanescent field spectroscopy on cold rubidium atoms (Sec. 5.6.3).

MOT parameter	**Value**
Diameter d_{MOT}	3.5 mm
Number of atoms N_0	6.33×10^7
Density ρ_{MOT}	2.82×10^9 per cm^{-3}

Table 5.2: Parameters of our ^{87}Rb MOT

5.6 Interfacing of MOT and nanofiber in UHV

5.6.1 Overlap of MOT and nanofiber

The center of the trap can be moved independently in each of the dimensions x, y, z by controlling the current in the corresponding compensation coil. Also, the TNF can be moved inside the vacuum chamber by using the adjustable millimeter screw as discussed in Sec. 4.2.3 of Chapter 4. Combining the two aforementioned techniques, the MOT is overlapped with the TNF inside the vacuum chamber (verified by images captured from two different angles with CCD camera and webcamera) . Fig. 5.16 shows the overlapping of MOT and TNF as captured by the CCD camera. This is done while keeping the blue laser coupled into the TNF with a power of at least 5 μW. The blue laser power can be increased to 200-300 μW without causing any damage to TNF. However, a further increase in blue power may potentially damage the TNF.

Number of atoms in the close neighborhood of nanofiber

With the knowledge of the atomic cloud density and dimensions of nanofiber, it is possible to find the number of atoms in the close neighborhood of TNF that can be addressed by the guided mode via the evanescent field of nanofiber. The number of atoms N_{TNF} in the

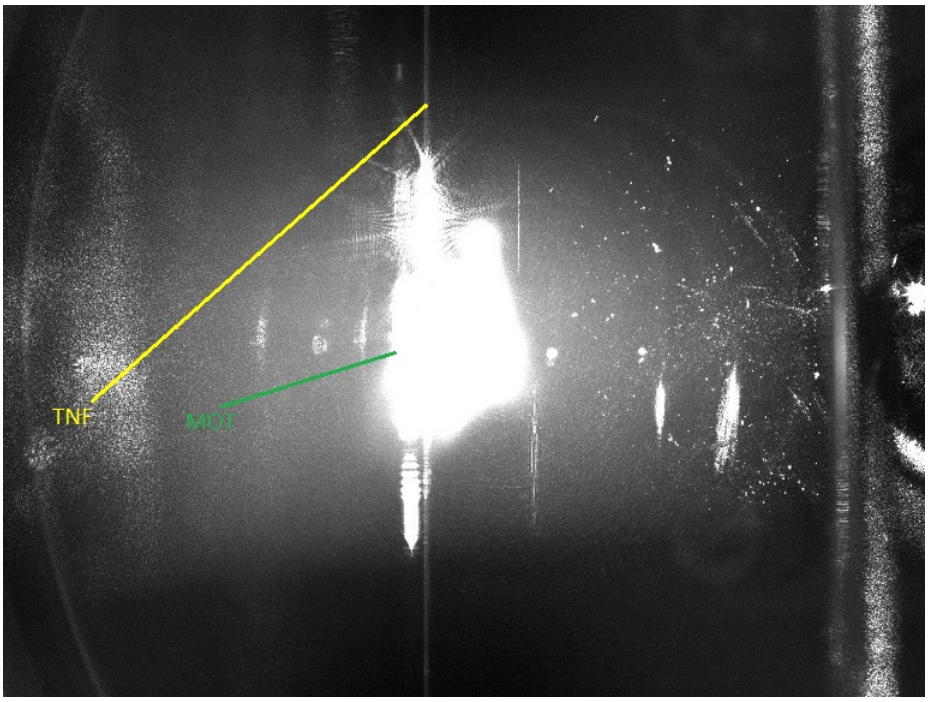

Figure 5.16: Overlap of MOT and TNF

vicinity of nanofiber is given by,

$$N_{TNF} = L_w \pi [a_{TNF} + \Lambda_{11})^2 - a_{TNF}^2] \rho_{MOT} \tag{5.4}$$

where TNF waist $L_w = 2$ mm, TNF radius $a_{TNF} = 200$ nm are obtained from Table 4.2 in Chapter 4 and MOT density from Table 5.2. The decay length for the fundamental mode $\Lambda_{11} = 170$ nm has been calculated by Eq. (2.19) in Sec. 2.2.2 of Chapter 2. Substituting all the values, $N_{TNF} = 2$.

Unfortunately in our case, only a very few atoms ~ 2 are in the vicinity to have interaction with the evanescent field of nanofiber.

If a resonant probe laser field is coupled into the TNF for evanescent field spectroscopy on cold rubidium atoms, its power has to be low enough so as not to saturate these 2 atoms in the neighborhood of nanofiber. It is reasonable to assume that both these atoms are in the ground state since the MOT beams and the magnetic field are switched off during the

probing. The probe power, P_{pr} can be estimated as

$$P_{pr} = \frac{hc}{\lambda}\Gamma N_{TNF} \tag{5.5}$$

where $\Gamma = 38.11$ MHz is the decay rate for D2 transition of ^{87}Rb and $\lambda = 780.246$ nm is the resonant probe wavelength. Substituting the values, the probe laser power $P_{pr} = 17$ pW. Thus, in principle for probing approximately 2 atoms around nanofiber , a weak probe power ≤ 17 pW has to be sent through TNF for observing some absorption signal. There are experimental difficulties which I will discuss in Sec. 5.6.3.

5.6.2 Coupling of atomic fluorescence into the guided mode of nanofiber

A single photon counting module (SPCM) is used for measuring the fluorescence of the MOT through TNF. A patch cable, spliced to one end of the TNF, is connected to a fiber out-coupler. The light coming out of the out-coupler is collimated and made to pass through a set of red filters. After the filters, a lens is put in the beam path to focus the fluorescence photons into the SPCM. The SPCM is not fiber-coupled and hence put inside a black box with a tiny hole. This part of the setup can be seen in Fig. 5.9. The red filters allow the fluorescence photons to pass through while blocking out the blue laser beam, even though the blue cannot be completely eliminated giving rise to additional photon counts in SPCM. The mean photon counts are recorded for four conditions. During the first 20 seconds, the background room light along with dark counts give a mean number of counts of 1 ± 0.5 KHz. For the next 20 seconds, the blue laser (power 10 μW) is turned on and coupled into the TNF giving a mean number counts of 50 ± 10 KHz. For the following 20 seconds, the MOT beams are switched on and 150 ± 10 KHz was registered in SPCM. For the final 20 seconds, the magnetic field is switched on and the MOT is overlapped with TNF. A mean total number of counts of 250 ± 10 KHz was observed. Thus, an increase of 10^5 counts/s above the scattering background is observed and it accounts for the coupling of the MOT fluorescence into the guided mode of TNF.

The fluorescence photon count rate n_p can be estimated as [48],

$$n_p = N_e R_{scat} \eta_{fiber} T_{fiber} \eta_D \tag{5.6}$$

where N_e is the effective number of atoms in excited state around nanofiber, R_{scat} is the atomic scattering rate, T_{fiber} is the fiber transmission from the mid to one end, η_D is the detector quantum efficiency and η_{fiber} is the averaged coupling efficiency of the spontaneous emission to the guided mode. With all the values, $n_p = 10^5$, $N_e = 1$ ($N_e = \frac{N_{TNF}}{2}$ since approximately half of the atoms in MOT are in excited state), $\eta_D = 30\%$ (including losses from filters), $R_{scat} = 1.8 \times 10^7\ s^{-1}$, $T_{fiber} = 80\%$ one obtains $\eta_{fiber} = 2.3\%$ using Eq. (5.6). Therefore, one can efficiently collect the fluorescence of a few atoms through the nanofiber. The interesting point to note is that the fluorescence photons from such a small number of atoms can be observed under a circumstance when a large number of photons (order of 10^{16} photons/s) from the MOT beams are irradiating the nanofiber.

Due to the modification of the vacuum modes in the presence of strongly guided fundamental (HE_{11}) mode, the spontaneous emission rate of an atom is enhanced in the vicinity of a nanofiber.

$$\gamma_{total}(r) = \gamma_{free}(r) + \gamma_{guid}(r) \tag{5.7}$$

The full quantum theoretical treatment of spontaneous emission for a cesium atom near a nanofiber can be found in [40]. The results of that analysis show the fractional spontaneous decay rate into guided mode of TNF can be as high as 28% for atoms on the surface of nanofiber and 4% for atoms at one radius away from the nanofiber surface. This happens at an optimal value $k_0 a = 1.45$ and we are reasonably close to the optimum with our nanofibers.

5.6.3 Attempt to see absorption of a probe beam through nanofiber by MOT cloud

The goal is to observe interaction of atoms with the fiber-guided light via evanescent field of the TNF. First, a good overlap between the MOT and the nanofiber is ensured after which the probe laser is coupled into the TNF. The probe beam coupling out of the other end

of the TNF is made to pass through a set of red filters and focussed ,by a lens, onto an avalanche photodetector (APD). The purpose of the filters is to eliminate the blue laser as already discussed. We have tried evanescent field spectroscopy on cold rubidium atoms, first without switching on-off the MOT beams, the magnetic field and the probe beam and then switching them in a particular sequence (Fig. 5.14). So far, we have not been able to observe any absorption signal with our current methods and techniques. I describe our challenges and difficulties below.

First of all, it is hard to detect low power $\approx$ 17 pW (calculated in Sec. 5.6.1) with our avalanche photodetector (APD), which can only measure down to $200 - 300$ pW. Any power below that has a poor signal to noise ratio. If a somewhat detectable power ($\approx$ 100 pW) is sent through TNF, there is a strong likelihood of saturating the few atoms in the neighborhood of nanofiber. Our efforts to integrate the photon counts from SPCM to obtain a macroscopic absorption signal did not succeed. This is because of the shot noise (on the order of $\sqrt{N}$ for N photons detected) in the signal and other electronic problems we encountered. Currently, we are developing a technique called heterodyne measurement for detection of ultra-low powers on the order of ten picowatts. In this technique, the free-space local oscillator beam is made to overlap with the probe signal through the nanofiber on a beam splitter and the interference fringes are observed by a balanced detector. Any change in the visibility of fringes will be a sign of absorption of probe beam through the nanofiber.

Secondly, the different kind of switches (discussed in Sec. 5.4) have been developed primarily for this experiment. It is important not to influence the atoms by the MOT beams and the magnetic field during evanescent field spectroscopy. MOT beams, if kept on, will deplete the ground-state population of atomic ensemble and may saturate the atoms around the nanofiber. The magnetic field, if not switched off, will cause a Zeeman splitting of the spectral line for the atoms in the MOT and may reduce the probability of the atoms around nanofiber to absorb a photon. The probe beam, if kept on, may saturate the few atoms

around the nanofiber or may even push the atoms further away from the nanofiber surface. Hence, the MOT beams, the magnetic field and the probe beam all are switched on-off in the timing sequence shown in Fig. 5.14.

Thirdly, when the MOT is overlapped with the nanofiber, the density of cloud decreases around the nanofiber [51]. This can be explained as follows. The temperature of the nanofiber is higher than the MOT temperature and hence when both of them are overlapped, the trap around nanofiber becomes shallow with fewer atoms owing to a rise of temperature in that region by few hundreds of μK. Also, photons from MOT beams that are reflected of nanofiber surface, may get scattered by a nearby atom. This can affect the MOT trapping potential adversely in the close neighborhood of the nanofiber. All these effects may lead to a reduction of the number of atoms in the vicinity of the nanofiber.

Finally, it is hard to overlap the waist of nanofiber with the densest region of MOT. This is because it is not possible to pinpoint the taper waist by looking at the TNF visually or by a CCD camera. Moreover, when the MOT cloud is moved around by the compensation coils to coincide with nanofiber waist, it often gets distorted in shape making it harder for anyone to identify the densest part of MOT. Also, the limitation of our nanofiber is it has short waist of 1-2 mm. This waist can be made longer by modifying the fabrication technique. By using 'flame-brushing technique' (discussed in Chapter 6) it can be possible to obtain nanofibers with longer taper waist.

A few other research groups working with cold atoms and nanofibers have been able to see the absorption through the nanofiber by the atomic cloud in last few years or so. Around 30% absorption through the nanofiber by the cold cesium atoms was reported by the group of A. Rauschenbeutel [51]) back in 2007. There is hope and belief that we may not be too far away from hitting the jackpot.

Chapter 6

Conclusion and Outlook

In my thesis, I have presented in detail our efforts in building up the MOT-nanofiber interface from scratch. At the initial stage, there are two parts to this experiment. I was myself involved in fabrication, characterization of nanofibers and the process of transferring it from fiber-pulling rig to our vacuum chamber. The other part of the experiment i.e., setting up of the trap and obtaining the MOT cloud was initially carried out by my colleagues till I joined them with the nanofiber inside UHV. The absorption of a free-space beam by the MOT cloud helped to estimate some important parameters like the cloud density and the number of trapped atoms. We have a relatively big MOT size ($\sim$ 3.5 mm) to facilitate good overlap with the nanofiber. It may be helpful to tune the probe laser frequency to a different transition in ^{87}Rb for evanescent field spectroscopy on the cold atoms. This will eliminate any effect of the MOT beams on the probe spectroscopy. More investigation needs to be done on pulse duration and delay with regards to switching on-off the MOT beams, the magnetic field and the probe beam. Undoubtedly, it is challenging to interact with the atoms via evanescent field since our calculations show there are few (≈ 2) atoms in the close neighborhood of TNF that can be addressed by the probe field. This number is limited by the atomic density and the length of taper waist. The density of cloud can be increased by the compression of the MOT which requires shooting up the current in the main coils, within a limit (otherwise the wires will melt). Another convenient experimental approach is to fabricate nanofibers with a longer taper waist. This can be achieved by 'flame brushing technique' [47], where the translation stages, with the fiber clamped onto it, are moved back and forth through the flame during the fiber-pulling process. In this way, one can fabricate nanofiber with waist as long as 10 mm [49].

The power handling capability of our nanofiber is typically $\sim 250-300$ μW. If more power is injected into TNF, it will lead to its damage. This is because the TNF is not completely free of smaller dust particles and whatever dust is sticking to the surface of nanofiber cannot be removed by the usual cleaning procedure. However, with improved facilities [38] it can be possible to fabricate nanofibers which can handle power of atleast tens of mW, if not more. One has to ensure that during fiber-pulling and transfer procedures the fiber taper is exposed to only clean air or vacuum. This is possible if everything is done inside a clean room or in a similar enviroment, like using N_2 purge to blow away the dust may work. Also, it is recommended to use a purified mixture of hydrogen and oxygen in right proportion for the flame. It is also important to put the fiber-pulling rig on a highly stable, anti-vibration platform (like Granite slab) to remove any external vibration from hampering the pulling process. We are currently working on improving the existing fiber-pulling facilities to accommodate the demands of fabricating a more robust nanofiber with high power handling capability.

With these robust nanofibers, one can proceed towards trapping atoms by creating a two-color evanescent field dipole trap around the nanofiber (discussed in Chapter 1). The atoms from the MOT will have to be transferred to this trap around nanofiber. One of the immediate goals would be to observe electromagnetically induced transparency (EIT) in the system of trapped atoms by coupling the 'signal' and the 'control' fields into the nanofiber. In EIT, the control field, tuned near resonance to a transition, will create a spectral 'window' of transparency in the absorption spectrum of the signal field which is tuned near resonance to a different transition, provided the three levels are selected properly. A good EIT result will most likely result in a publication for us. Many other possible experiments based on our MOT-nanofiber interface have been proposed previously in Chapter 1.

A drawback in using a tapered nanofiber is that surface interactions such as van der Waals and Casimir-Polder come into play and can affect both the resonance line shape and

the central peak with respect to free-space spectroscopy. Although there are theoretical investigations done to understand the influence of these surface interactions, further exploration through experiments is required.

Appendix A

Components

A.1 External cavity diode lasers (ECDLs)

All the lasers (cooling, repumping and probe) used in our experiment are diode lasers assembled using homemade units. The design principle is based on Littrow configuration [52]. The current and temperature of the laser are controlled by Thorlabs unit ITC102 (usuallly referrred to as TEC), which have built in proportional-integral-derivative (PID) temperature controller circuit and current limiting circuit. Temperature sensors (AD590) provide reading to the PID controllers, which in turn control the current through the Peltier elements to cool or heat the diode. The output of the laser diode falls on a holographic diffraction grating to form an external cavity. The first-order diffraction is reflected back into the diode to provide optical feedback while the zeroth-order is reflected off a mirror to the output port. The angle of grating can be changed by a pizoelectric actuator. This allows the scanning of the laser frequency over a few Gigahertz range. The piezo signal is provided by a homemade controller circuit which generates a ramp signal of 60V range (adjustable). The ECDL's emission frequency can be controlled independently by three means:

1. The laser frequency can be coarse-tuned by two screws: one horizontal screw, attached to the piezoelectric element for controlling the horizontal angle of grating, and the vertical screw, attached to the platform beneath the grating for controlling the vertical angle control of grating. This is a starting process for tuning the laser close to a desired frequency.

2. Changing the temperature of the laser diode via TEC causes the Fabry- Perot cavity to expand and in turn the refractive index of the material changes. In

this way the laser frequency can be tuned. Usually, the temperature is set to some stable constant value and it is not touched unless one has exhausted other options of tuning the laser frequency.

3. The laser diode current is dependent on the emission frequency. This is because in a semiconductor (diode) laser, the excitation of the gain medium depends on the current injected into the junction region of a forward biased diode. Changing the laser current offers a fastest way to influence the laser frequency. By trial and error, one has to find a current value for obtaining a stable desired laser frequency.

The process of tuning our homemade lasers is tedious and may take a long time, ranging from few days to several weeks. Once the stable parameters (current and temperature) are found for a desired wavelength then the job is comparatively less difficult to tune it back to that wavelength.

A.2 Tapered amplifier (TA)

A tapered amplifier is a semiconductor diode in which a gain amplifies the input coherent field. It requires a similar temperature and current control units to that of an ECDL, only with higher current capacity (2 A). Its amplification varies with input power and for low powers the amplification is higher. For a free-space input of 5 mW, we get an output of 360 mW. Due to its rectangular spatial mode, the beam is subjected to mode cleaning right after it has passed through.

A.3 Acousto optic modulator (AOM)

An AOM is a device which shifts the laser frequency by making use of acoustic waves in a crystal. The output of an AOM has several diffraction orders which allows the user to pick

the order of frequency shift as needed. A sine wave with a frequency within the bandwidth of AOM, is fed to a RF amplifier, which amplifies the signal by almost 10 dB. This amplified signal is required to operate the AOM and any modulation on this signal will be reflected on the AOM output.

A.4 Lock-in amplifier

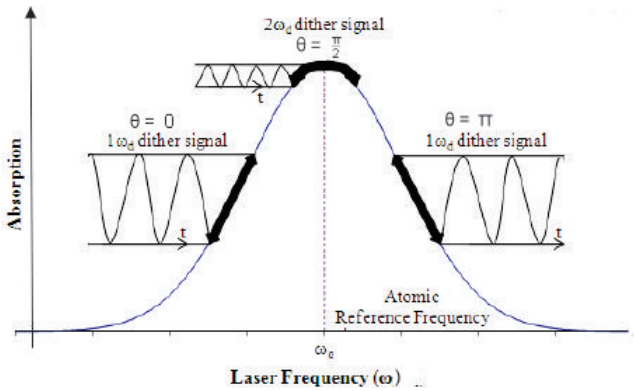

Figure A.1: Locking mechanism

The atomic absorption spectrum (shown in Fig. A.1) has the form of a Lorentzian function

$$L(x) = \frac{1}{1+x^2} \tag{A.1}$$

where $x \propto \omega - \omega_0$, ω is the laser frequency and ω_0 is the atomic reference frequency. Using Taylor's series expansion for small values of x,

$$L(x) = \begin{cases} 1 - x^2 & (x \sim 0) \\ \frac{1}{2} - \frac{x}{2} & (x > 0) \\ \frac{1}{2} + \frac{x}{2} & (x < 0) \end{cases} \tag{A.2}$$

Since a dither signal ($V_{dither} = B\sin[\omega_d t]$) is applied to the piezo of the laser, the laser frequency is modulated by it such that $x \propto \sin(\omega_d t)$. The modulated spectroscopic signal V_{in} is sent to one of the inputs of the lock-in amplifier. Substituting $x = K\sin(\omega_d t)$ (where

K is the proportionality factor) in Eq. (A.2), V_{in} has the form,

$$V_{in} = \begin{cases} 1 - \frac{K}{2} + \frac{K}{2}\cos(2\omega_d t) & (\omega \sim \omega_0) \\ \frac{1}{2} - \frac{K\sin(\omega_d t)}{2} & (\omega > \omega_0) \\ \frac{1}{2} + \frac{K\sin(\omega_d t)}{2} & (\omega < \omega_0) \end{cases} \tag{A.3}$$

The high pass filter (refer to Fig. A.2) removes the dc components in Eq. (A.3). Therefore, we can rewrite Eq. (A.3) by introducing a phase factor θ to differentiate the three regions in the absorption peak as shown in Fig. A.1.

$$V_{in} = \begin{cases} A\sin(\omega_d t + \theta) & (\theta = 0) \\ A\sin(2\omega_d t + \theta) & (\theta = \pi/2) \\ A\sin(\omega_d t + \theta) & (\theta = \pi) \end{cases} \tag{A.4}$$

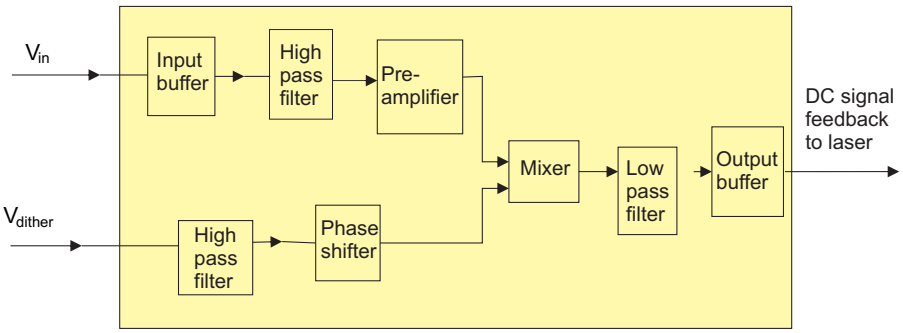

Figure A.2: Schematic of lock-in amplifier

V_{in} and V_{dither} with same amplitude and phase (ensured by phase-shifter) are mixed in

the mixer. The output of the mixer is

$$V_{mixed} = \begin{cases} \frac{AB}{2}[\cos\theta - \cos(2\omega_d t + \theta)] & (\theta = 0, \pi) \\ \frac{AB}{2}[\cos(\omega_d t + \theta) - \cos(3\omega_d t + \theta)] & (\theta = \pi/2) \end{cases} \tag{A.5}$$

After the mixer, the low pass filter only allows the dc signal to pass through. This cancels out all the time varying cosine terms in Eq. (A.5).

When the laser frequency is not on resonance with the atomic reference frequency i.e. $\theta = 0$ or π, one dither cycle produces a ω_d absorption signal which results in a positive (for $\theta = 0$) or negative (for $\theta = \pi$) error signal being fed back to the laser (Eq. (A.5)).

When the laser frequency is on resonance with the atomic reference frequency i.e. $\theta = \pi/2$, one dither cycle passes twice over the the absorption peak producing a $2\omega_d$ absorption signal which results in a zero error signal being fed back to the laser (Eq. (A.5)).

In this way, the laser frequency ω is locked to the atomic reference frequency ω_0 by using lock-in amplifier.

A.5 Voltage-controlled oscillator (VCO)

A voltage-controlled oscillator is an electronic oscillator whose output oscillation frequency is controlled by an input voltage. The effect is instantaneous so that any modulating voltage signal will result in a frequency-modulated or phase-modulated output from VCO. We use it in out experiment to scan the probe laser. The output of VCO is a frequency-modulated signal used to drive an AOM (via RF amplifier).

Appendix B

Micro-macro entanglement of light

Title: *Observation of micro-macro entanglement of light*

Authors: *A.I. Lvovsky, R. Ghobadi, A. Chandra, A.S. Prasad and C. Simon*

Journal: *Nature Physics 9,541-544 (2013)* [53]

I was involved in this experiment before starting the cold-atoms-nanofiber project discussed so far. 'Observation of micro-macro entanglement of light' has been published in Nature Physics and I am a co-author in this paper. I will briefly talk about this experiment. From a heralded single photon source [33] (using non-degenerate spontaneous parametric down-conversion (SPDC) in PPKTP crystal) single photon states are generated in our lab with a probability of 55-60 % (uncorrected for losses). A single photon state is made incident on a beam splitter and separated into two modes (say Alice's mode and Bob's mode), shown in Fig. B.1. In the first part of the experiment, Bob's mode is displaced in phase space, which converts it to a macroscopic state, and its photon number statistics are measured by a balanced detector. At the same time, the quadratures are measured by a homodyne detector at Alice's end. It has been observed that Alice's quadrature measurement clearly influences the photon statistics measurement for Bob. The two macroscopically different states at Bob's end, which are in quantum superposition represent the 'dead' and 'alive' states of the Schrodinger cat.

In the next part of the experiment, the macroscopic (displaced) state at Bob's end is undisplaced in phase space and converted back to microscopic state. Subsequently, quantum homodyne tomography is performed at both ends and the two- mode density matrix is reconstructed. The results from reconstruction show these two channels are entangled.

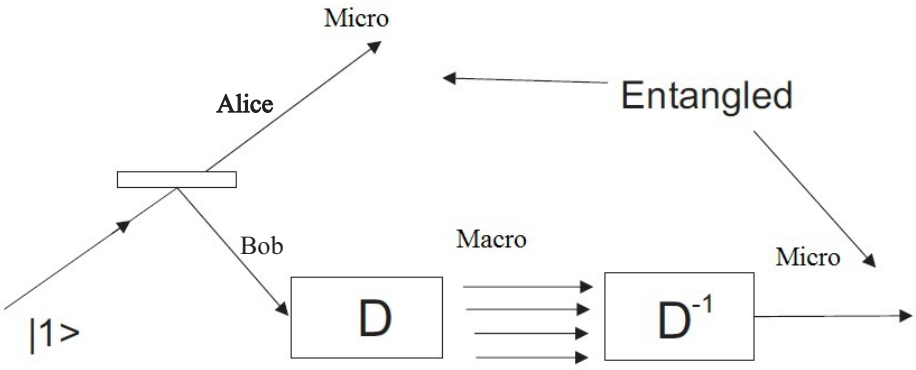

Figure B.1: Scheme for micro-macro entanglement of light. D denotes the displacement in phase space (local operation).

Since entanglement can neither be created or destroyed by local operation, this implies the microscopic and macroscopic states have been entangled.

I contributed to this experiment by helping with the optical alignment in the setup. I also performed some calculations and plottings as was necessary. This generation of Schrodinger cat states, as also done by others, seem to suggest that quantum mechanics may apply on all scales, be it microscopic or macroscopic.

Bibliography

[1] A. Reiserer, N. kalb, G. Rempe, S. Ritter, *A quantum gate between a flying optical photon and a single trapped atom*, Nature 508, 237-240 (2014).

[2] T. Tiecke, J. Thompson, N. Leon, L. Liu, V. Vuletic, M. Lukin *Nanophotonic quantum phase switch with a single atom*, Nature 508, 241-244 (2014).

[3] G. Nogues, A. Rauschenbeutel, S. Osnaghi, M. Brune, J. M. Raimond and S. Haroche, *Seeing a single photon without destroying it*, Nature 400, 239-242 (1999).

[4] S. Kuhr, W. Alt, D. Schrader, M. Muller, V. Gomer and D. Meschede, *Deterministic Delivery of a Single Atom*, Science 293, 278 (2001).

[5] L. Duan, M. Lukin, I. Cirac and P. Zoller, *Long-distance quantum communication with atomic ensembles and linear optics* , Nature 414, 413-418 (2001).

[6] S. Choi, H. Deng, J. Laurat and H. J. Kimble, *Mapping photonic entanglement into and out of a quantum memory*, Nature 452, 67-71 (2008)

[7] C. Hood, T. Lynn, A. Doherty, A. Parkins and H. Kimble,P. Pinkse, T. Fischer, P. Maunz and G. Rempe *The Atom-Cavity Microscope: Single atoms Bound in Orbit by Single Photons*, Science 287, 5457 (2000)

[8] P. Pinkse, T. Fischer, P. Maunz and G. Rempe *Trapping an atom with single photons*, Nature 404, 365-368 (2000)

[9] J. Raimond, M. Brune and S. Haroche *Manipulating quantum entanglement atoms and photons in a cavity*, Rev of Mod. Phys. 73 (2001)

[10] T. Aoki, B. Dayan, E. Wilcut, W. Bowen A. Parkins, T. Kippenberg, K. Vahala and H. Kimble, *Observation of strong coupling between one atom and a monolithic microresonator*, Nature 443, 671-674 (2006)

[11] J. Bochmann, A. Vainsencher, D. Awschalom, A. Cleland *Nanomechanical coupling between microwave and optical photons*, Nature Physics 9, 712-716 (2013)

[12] H. Kimble, The quantum internet, Nature 453, 123-1030 (2008)

[13] M, Nielsen and I. Chuang, Quantum Computaion and Quantum Information, Cambridge University Press 2010.

[14] P Palittapongarnpim, *Characterization of magneto-optical trap for experiments in light-atom interfacing, Master's thesis*, , University of Calgary (2012).

[15] C. J. Foot, *Atomic Physics*, , Oxford University Press 2011.

[16] B. Saleh, M. Teich *Fundamentals of Photonics*, Wiley 2007.

[17] G. Sague, *Cold atom physics using ultra-thin optical fibers, PhD thesis*, Rheinischen Friedrich-Wilhelms-Universitat Bonn (2008).

[18] H. Metcalf and P. Straten, *Laser cooling and trapping*, Springer-Verlag New York (1999).

[19] T. Okoshi, *Optical Fibers*, Academic Press Inc. (1982).

[20] K. Nayak and K. Hakuta, *Single atoms on an optical nanofibre*, New J. Phys, 10, 053003 (2008).

[21] A. Yariv and Y. Pochi, *Photonics: Optical Electronics In Modern Communications*, 6th ed., Oxford University Press (2006).

[22] E. Vetsch, *Optical interface based on a nanofiber trap atom-trap, PhD thesis*, Johannes Gutenberg-Universitat in Mainz, (2010).

[23] Lucia Duca, *Implementation and testing of a magneto-optical trap for neutral ^{87}Rb atoms for quantum information processing, Master's thesis*, Alma Mater Studiorum - Universita' di Bologna (2009).

[24] A. Hartung, S. Brueckner, H. Bartelt, *Limits of light guidance in optical nanofibers*, Optics Express 18, 3754-3761 (2010).

[25] F. Warken and H. Giessen, *Fast profile measurement of micrometer-sized tapered fibers with better than 50-nm accuracy* , Optics Letters 29, 1727-1729 (2004).

[26] M. Juarez and P. Oxley, *The Use of a Lock-in Amplifier to Stabilize the Frequency of a Diode Laser, Honors Thesis*, (2009) `http://college.holycross.edu/faculty/poxley/pubs/Miguel_Honors_Thesis.pdf`.

[27] H. Schmidt and A. Imamoglu, *Giant kerr nonlinearities obtained by electromagnetically induced transparency*, Optics letters 21(23):1936-1938, (1996).

[28] J. Gea-Banacloche, *Impossibility of large phase shift via the giant kerr effect with single-photon wave packets*, Phys. Rev. A, 81:043283, (2010)

[29] B He, A. Macrae, Y. Han, A. lvovsky and C. Simon, *Transverse multimode effects on the performance of photon-photon gates*, Phys. Rev. A 83:022312, (2011)

[30] S. van Enk and H. Kimble, *Single atom in free space as a quantum aperture*, Phys. Rev. A 61, 051802 (2000)

[31] V. Balykin, K. Hakuta, F. Kien, J. Liang and M. MOrinaga, *Atom trapping and guiding with a subwavelength-diameter optical fiber*, Phys. Rev. A 70, 011401(R), (2004)

[32] F. Kien, V. Balykin and K. Hakuta *Atom trap and waveguide using a two-color evanescent light field around a sub-wavelength diameter optical fiber*, Phys. Rev. A 70, 063403 (2004).

[33] N. Jain, *Quantum optical state engineering at the few photon level, M.Sc. thesis*, University of Calgary (2009)

[34] F. L. Kien, J.Q. Liang, K. Hakuta, V. I. Balykin, *Field intensity distributions and polarization orientations in a vacuum-clad subwavelength-diameter optical fiber*, Optics Communications 242, 445-455 (2004).

[35] H.C. van de Hulst, *Light Scattering by Small Particles*, Wiley, New York (1957).

[36] D.J. Butler and G.W. Forbes, *Fiber-diameter measurement by occlusion of a gaussian beam*, Applied Optics 37, 2598-2606 (1998).

[37] E.R. Abraham and E. Cornell, *Teflon feedthrough for coupling optical fibers into ultra-high vacuum systems*, Applied Optics 37, 1762-1763 (1998).

[38] J. Hoffman, S. Ravets, J. Grover, P. Solano, P. Kordell, J. W-Campos, L. Orozco, S. Rolston, *Ultrahigh Transmission Optical Nanofibers*, preprint arXiv:1405.3258 (2014).

[39] A. Gorban, K. Choi, D. Alton, D. Ding, C. Lacroute, M. Pototschnig, T. Thiele, N. Stern, H.J. Kimble, *Demonstration of a State-Insensitive, Compensated Nanofiber Trap*, PRL 109, 033603 (2012).

[40] F. Kien, S. Gupta, V. Balykin and K. Hakuta, *Spontaneous emission of a cesium atom near a nanofiber: Efficient coupling of light to guided modes*, Phys. Rev. A 72, 032509 (2005).

[41] E. Vetsch, D. Reitz, G. Sague, R. Schmidt, S. Dawkins and A. Rauschenbeutel, *Optical interface Created by laser-cooled Atoms trapped in the Evanescent Field Surrounding an Optical nanofiber*, PRL 104, 203603 (2010).

[42] E. Raab, M. Prentiss, A. Cable, S. Chu and D. Pritchard, *Trapping of neutral Sodium Atoms with Radiation Pressure*, PRL 59, 2631 (1987).

[43] Y. Band, *Light and matter: Electromagnetism, optics, spectroscopy and lasers*, Chapter 9, John Wiley and Sons (2006).

[44] P. Bouyer, P. Lemonde, M. Dahan, A. Michaud, C. Salomon and J. Dalibard An Atom Trap Relying on Optical Pumping, Europhys. Lett. 27 569-574 (1994).

[45] D.A. Steck, *Rubidium 87 D Line Data* (2001).

[46] T. Birks and Y. Li, *The Shape of Fiber Tapers*, Jour. of Lighwave Technology 10, 432 -438 (1992).

[47] F. Orucevic, V. L. Seguin, J. Heare, *Transmittance and near-field characterization of sub-wavelength tapered optical fibers*, Optics Express 15, 13624-13629 (2007).

[48] K. Nayak, P. Melentiev, M. Morinaga, F. Kien, V. Balykin and K. Hakuta, *Optical nanofiber as an efficient tool for manipulating and probing atomic fluorescence*, Optics Express 15, 5431-5439 (2007)

[49] D.J. Alton, *Interacting single atoms with nanophotonics for chip-integrated quantum networks, PhD thesis*, California Institute of Technology (2013).

[50] H. Lo, Y. Chen, P. Su, H. Chen, J. Chen, Y. Chen, I. Yu and Y. Chen, *Electromagnetically-induced-transparency-based cross-phase-modulation*, Phys. Rev. A 83, 041804(R) (2011).

[51] G. Sague, E. Vetsch, W. Alt, D. Meschede and A. Rauschenbeutel, *Cold-Atom Physics using Ultrathin Optical Fibers: Light-Induced Dipole Forces and Surface Interactions*, PRL 99, 163602 (2007).

[52] Design and Characterization of a Littrow Configuration External Cavity Diode Laser, `http://holoforum.org/data/pdf/aa-Collection_a_k/aa-Laser/aa_ECDL/ECDL-Littrow-Hong-Wenxian-caltech.pdf`.

[53] A. Lvovsky, R. Ghobadi, A. Chandra, A. Prasad and C. Simon, *Observation of micro-macro entanglement of light*, Nature Physics 9, 541-544 (2013).